THE SYNTHESIS OF ATOMICALLY THIN PT MONOLAYER TO MULTILAYER PT FILMS ON GRAPHENE AND MOS_2

A Thesis
Presented to
The Academic Faculty

by

Christopher Arnold

In Partial Fulfillment
of the Requirements for the Degree
Master of Science in the
School of Materials Science and Engineering

Georgia Institute of Technology
May 2018

THE SYNTHESIS OF ATOMICALLY THIN PT MONOLAYER TO MULTILAYER PT FILMS ON GRAPHENE AND MOS_2

Approved by:

Dr. Faisal Alamgir, Advisor
School of Materials Science and Engineering
Georgia Institute of Technology

Dr. Matthew McDowell
School of Materials Science and Engineering
Georgia Institute of Technology

Dr. Antonia Antoniou
School of Mechanical Engineering
Georgia Institute of Technology

Date Approved: [April 09, 2018]

ACKNOWLEDGEMENTS

It is my pleasure to acknowledge, Dr. Faisal Alamgir, my advisor, for providing his support and wisdom during my studies and research at Georgia Institute of Technology. The investment he made in terms of time and energy on my behalf were critical to my development and success as a researcher. I would also like to recognize my lab mates, Ali Abdelhafiz, Matthew Drexler, Crystal Bell, and Ankit Kuchhangi for their valuable input and stimulating discussions.

Matthew Drexler, Neha Kondekar, and Dr. Josh Kacher have all made significant contributions to this work via the X-ray photoelectron spectroscopy data collection, transmission electron microscopy imaging, and sample preparation. Therefore, I would like to thank them for their support. Additionally, I would like to thank Thomas Samuels and Dr. Jamie Warner at the University of Oxford for preparing and characterizing the graphenated Ni foam samples used for this thesis work.

Finally, I am grateful to my wife, parents, siblings, and friends for their constant support and encouragement through this entire process. They have helped me overcome numerous hurdles during my time at Georgia Tech., and I certainly would not have been as successful or sane throughout the last two years without them.

TABLE OF CONTENTS

LIST OF TABLES

LIST OF FIGURES

LIST OF SYMBOLS AND ABBREVIATIONS

$\Delta\Phi$	difference in material work functions
CV	cyclic voltammetry
CVD	chemical vapor deposition
DI	deionized
ECSA	electrochemically active surface area
EDX	energy dispersive X-ray spectroscopy
FFT	fast Fourier transform
HER	hydrogen evolution reaction
HOR	hydrogen oxidation reaction
IFFT	inverse fast Fourier transform
LSV	linear sweep voltammetry
ML	monolayer/multilayer
MoS_2	molybdenum disulfide
OCP	open circuit potential
ORR	oxygen reduction reaction
PEM	proton exchange membrane
Pt/C	platinum on carbon black
Pt/GR/Ni	platinum on graphenated Ni
SEM	scanning electron microscopy
SLRR	surface-limited redox replacement
TEM	transmission electron microscopy
ΔU_p	potential shift

UPD	underpotential deposition
XPS	X-ray photoelectron spectroscopy

SUMMARY

In the area of catalysis, substantial research is aimed at exploring the influence of catalyst supports as well as the size and morphology of precious metal nanostructures on activity, selectivity, and durability. In the past decade, efforts have evolved into the deposition of highly wetted ML of precious metals onto various catalyst supports. Similar to the use nanoparticle films, ML growth significantly reduces precious metal loading—therefore improving material costs. Additionally, though, ML depositions optimize the interface interactions between catalytically active materials and their support to a greater degree than nanoparticle films, allowing precise tunability of electronic properties via ligand effects and strained overlayers. Previous work by our research group showed how a room-temperature electrochemical method (SLRR) for precious metal ML deposition can be used for putting Pt on Au films with and without a sandwich layer of graphene. This thesis work studies the efficacy of using this same technique, and another derived from it, for depositing Pt-ML on two unique substrates—three-dimensional graphene and MoS_2 thin films—and evaluates the resulting effects on electrocatalytic performance. The three-dimensional (3D) graphene sample was synthesized by precipitating graphene on an open-celled Ni foam before covering the surface with Pt. Optionally, the Ni can be removed via etching, leaving a free-standing graphene foam decorated with Pt. This presents an excellent contrast to samples with Ni intact, and introduces the opportunity for synthesizing ligand flexible catalysts. The MoS_2 was grown at various thicknesses to achieve both horizontally and vertically oriented thin films. Interestingly, this allowed for the concentration of available MoS_2 edge sites to influence the Pt deposition. Samples were

characterized using SEM, EDS, XPS, TEM, and electrochemical techniques. Their efficacy as electrocatalysts was evaluated using ORR for the graphene samples and HER for the MoS_2 samples.

CHAPTER 1. INTRODUCTION

1.1 Motivation

Substantial research has been aimed at exploring the influence of catalyst supports as well as the size and morphology of precious metal nanostructures on the key catalyst performance metrics of activity, selectivity, and durability. However, for reactions such as ORR, kinetics remain sluggish leading to inefficiency. This can prevent technologies like PEM fuel cells, a device that promise high efficiency and little to no harmful emissions, and where ORR is a key reaction, from being adopted for widespread commercialization. To better comprehend and address this, it is critical to understand the reaction mechanisms for ORR. One simple reaction pathway consists of three major steps (Equations 1.1, 1.2, and 1.3) (where * indicates a catalyst surface site). [1] [2]

$$^1/_2\, O_2 + * \rightarrow\ O^* \tag{1.1}$$

$$O^* + H^+ + e^- \rightarrow OH^* \tag{1.2}$$

$$OH^* + H^+ + e^- \rightarrow H_2O + * \tag{1.3}$$

Based on this pathway, it is apparent that oxygen must first bind to the catalyst surface and subsequently get released as H_2O (steps 1.1 and 1.3). These two mechanisms drive the effectiveness of the catalyst for ORR, and suboptimal performance on either end yields lower activity. The result is that the catalyst can either bind oxygen too strongly to its surface, making it difficult for the oxygen to leave, and causing it to take up potential

reaction sites, or else bind oxygen too weakly, making it difficult to break the diatomic oxygen bond so that a hydroxyl group can form.

Sabatier's principle asserts that finding the perfect balance between these two leads to optimization of the catalyst and reactant interaction. This Goldilocks-like theory is not just applicable to ORR but generally holds true for any catalyst application. It can be graphically exemplified by a volcano plot, which plots activity versus adsorption energy for a given reactant. Figure 1.1 is of a volcano plot for ORR and clearly shows that both Pt and Pd are the best pure metal catalysts in terms of binding oxygen but would benefit from weaker binding with oxygen.

Additional hurdles toward adopting electrocatalyst based technologies for energy production include cost and durability of materials. Because precious metals remain the best possibilities in this context, catalysts can make up a significant portion of the overall cost in technologies that struggles to be cost competitive. Attempting to overcome this, most commercially available electrocatalysts utilize precious metal nanoparticles instead of bulk materials. For ORR and several other reactions, Pt nanoparticles are deposited on carbon black supports, a porous and chemically inert support. This approach lowers the amount of Pt incorporated in the catalysts and increases the ECSA, but it can significantly decrease durability as dissolution of materials, such as Pt and the carbon substrate, and Ostwald ripening begin to become problematic for maintaining catalytic activity during prolonged operation. Current catalyst research, which aims to reduce inefficiencies in activity and selectivity while lowering costs without sacrificing durability, has led to development of materials that significantly outperform current commercial catalysts. However, better comprehension of interactions at the interface between catalysts and

supports is still required for designing new materials. Moreover, this research remains fundamental, taking place on the nanoscale, without a pathway to widespread application. Therefore, new processing techniques are required to bring these high-performance catalysts to the macro-scale.

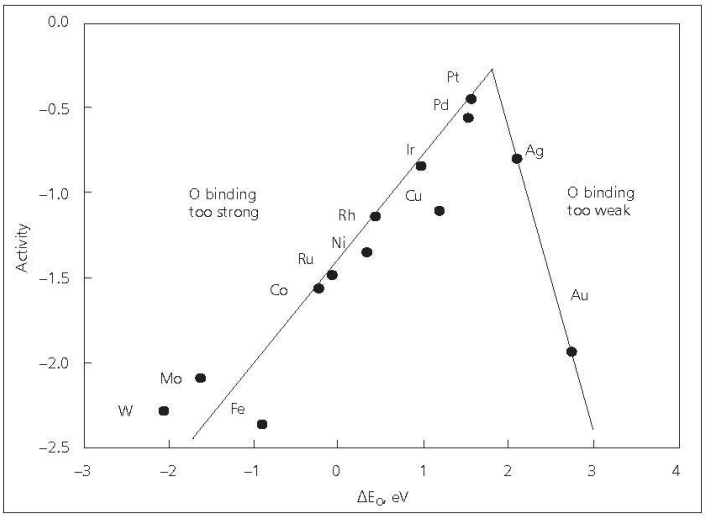

Figure 1.1 – Volcano plot displaying activity of pure metal catalysts for ORR based on theoretical calculations. (Reprinted with permission from [1]. Copyright 2004 American Chemical Society)

1.2 2D Materials

Two-dimensional (2D) materials are continuing to garner attention for their potential to further improve technologies that require minimal physical dimensions for improvement. [3] There is also significant research aimed at using 2D materials as heterogeneous catalysts and substrates for catalytically active nanomaterials. This is

because 2D materials boast a tremendous surface area to mass ratio, [4] [5] and often, they improve interface interactions as the support for precious metals.

The most well-known 2D material, graphene, originally obtained using adhesive tape to cleave graphite, has become one of the most heavily researched substances in materials science. [6] After the original production of single atomic layer graphene, bottom up production techniques such as CVD and epitaxial growth as well as top down methods such as mechanical and chemical exfoliation have been developed for more practical production. [7] Some work has even been done on synthesizing graphene in a roll-to-roll manner for scalable manufacturing. [8] The distinct attributes of graphene in the areas of mechanical stability, [9] electrical conductivity, [10] thermal conductivity, [11] high surface area to mass ratio, [4] and chemical inertness [12] make it a promising material for a wide variety of applications including catalysis, energy storage, and solar cells. For catalysis, graphene, or derivatives of it, acts as a promising heterogenous catalyst in its own right, but graphene truly excels as a support for catalytically active nanomaterials (e.g. Pt and Pd nanocrystals) in multicomponent catalysts.

The unique attributes of graphene make it an extremely stable support that facilitates high loading of precious metals. Furthermore, when graphene becomes modified through the presence of defects or inclusions it provides anchor points with strong bonding between graphene and deposited materials, allowing for excellent dispersion across the surface. [13] [14] Shang et al. highlighted the impact that graphene nanoflakes can have on MOR when decorated with Pt nanoparticles by comparing their catalyst to commercial Pt/C. [5] However, this work did not outline the mechanisms by which graphene affects catalytic properties. Subsequent work by our group investigated interactions between graphene and

deposited Pt, showing how graphene stains the Pt lattice, modifying its electronic properties as a function of the Pt overlayer thickness. In this way, graphene can tune the catalytic activity of Pt while also providing all the support benefits mentioned earlier.

Transition metal dichalcogenides, a group of 2D materials which have attracted attention for use in electronics owing to their direct band gaps, offer alternatives to graphene in terms of atomically thin catalysts and catalyst supports. MoS_2, one of the most prominent materials in this group, has displayed significant catalytic activity toward HER, [15] but, like graphene, stands out as a support in multicomponent catalysts that are used for applications such as HER, [16] MOR [17] [18], and water splitting [15]. A cursory review of literature indicates that less is known about the surface interactions between precious metals and MoS_2, compared to graphene, but theoretical calculations conclude that MoS_2 would provide numerous excellent anchoring points for materials such as precious metal nano-architectures. [19] [20]

1.3 Catalyst Enhancement

Several approaches have been taken to overcoming the sluggish ORR kinetics described earlier. One such method is creating nanoparticles of precious metal as opposed to bulk metals. Observations over several decades have indicated that for optimal ORR kinetics, nanoparticles should be approximately 3 nm in diameter. [21] [22] [23] However, improvements in kinetics associated with particle size may result more directly from improved ECSA to mass ratio and the distribution of crystal facets. This is supported by DFT calculations which indicate that certain surface morphologies have greater specific

activity than others. [24] Significantly scaling down the catalyst size also yields much less expensive catalysts resulting from the increased surface area to mass ratio. For these reasons, precious metal nanoparticles are still used reliably in most commercially available catalysts.

Additionally, interest has recently intensified for creating bimetallic catalysts (e.g. PtM, where M is a second metal) as a means of improving catalytic activity. The idea behind these catalysts is modifying the electronic properties of the main material participating in the catalytic reaction. Going back to Sabatier's principle, bulk metals can generally be improved in terms of bonding with reactants. Therefore, tuning the electronic properties of catalysts in the proper way, can optimize their activity. Examples of this kind of modification include alloying, synthesizing core-shell structures where monolayers of precious metal encase a core of the second metal, and layering where precious metal monolayers are deposited on film of the second metal. Frequently, with these catalyst constructions, the second metal will be much cheaper than the precious metal, and as a result, the material costs of these catalysts can be much lower than traditional pure precious metal catalysts.

Theoretical and experimental research in this area has identified that a catalyst's d-band center has a strong correlation with its activity. [25] In terms of Pt for ORR, a slightly down-shifted d-band center relative to the fermi level has shown greatly improved activity. [24] Two of the main contributors for modifying a catalyst's electronic properties in bimetallic constructions are strain and the so-called metal ligand effect. Pt benefits from stronger bonded core-shell electrons, and therefore, selecting metals that can induce a slight compression in the Pt lattice and/or drain charge from Pt are going to perform better than

bulk Pt. [26] This is exemplified by the volcano plots in Figure 1.2, where the red dots represent experimental observations, and the black dots represent DFT calculations.

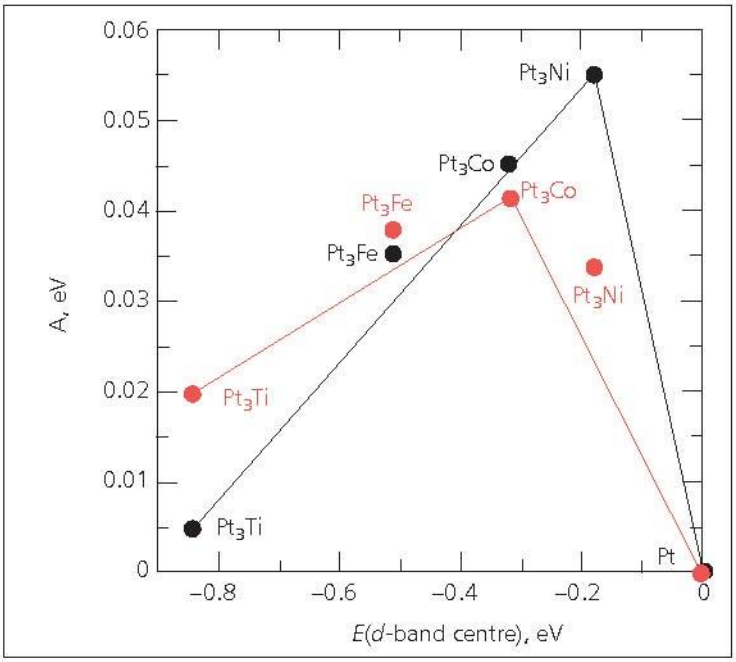

Figure 1.2 - Volcano plot displaying activity of bimetallic catalysts for ORR based on DFT calculations (black dots) and experimental observations (red dots). (Reprinted with permission from [25]. Copyright 2006 John Wiley and Sons)

1.4 Surface-Limited Redox Replacement

As mentioned already, decades of research have been aimed at investigating the catalytic activity and selectivity of precious metal nanoparticles compared to bulk metal electrodes. Earlier investigations into highly dispersed metal nanoparticles revealed that particle size has influence on the surface coordination number and the fraction of crystal faces (111) and (100). [22] [27] Both of these have been shown to dramatically influence

surface chemisorption. Further research in this area highlighted the role that catalyst supports begin to play in activity, selectivity, and durability once particle size is reduced sufficiently. For these reasons, precise control over particle growth and dispersion across substrates has been explored considerably, and more recently, 2D catalyst films have been investigated. Through a high degree of wetting, these 2D catalyst films can have remarkable specific surface areas and achieve high degree of interaction between the catalyst and the support, allowing for precision tuning of catalytic activity.

Electrodeposition has become one of the more popular techniques for creating well dispersed films of precious metals on a variety of substrates. Unfortunately, though, standard electrodeposition does not work well in all cases. Pt for instance, tends to form 3D clusters at defect sites during deposition owing to its high surface energy. [28] [29] Often to overcome this issue, surface-limited redox replacement (SLRR) can be employed. This technique, developed by Brankovic et al. [30], is comprised of two main steps that include (i) the epitaxial deposition of a sacrificial metal monolayer via UPD and (ii) the subsequent replacement of the sacrificial layer with a more noble metal at OCP (Figure 1.3). This two-step process can be repeated until the film reaches the desired thickness, with each new UPD layer going down on the noble metal layer previously deposited. The resulting film is generally much more uniform, ubiquitous, and precise compared to film growth carried out using standard bulk deposition. To understand why, it is important to take a closer look at the first step of the SLRR process—the UPD between the substrate and the sacrificial metal.

UPD is a unique phenomenon that occurs between pairs of materials, where a metal being electrodeposited can be reduced on a foreign substrate at a lower energy level (i.e.

higher potential) than the required energy for bulk reduction of the metal (i.e. Nernst potential). The existence of a UPD between pairs of metals was correlated with the difference in work functions of the two materials by Kolb et al. [31] in 1974. This work went on to develop a linear relationship between the difference in work functions and the shift in potential between bulk reduction and the UPD (equation 1.4).

$$\Delta U_p = \alpha \Delta \Phi \; with \; \alpha = 0.5 \; V \; eV^{-1} \tag{1.4}$$

After this correlation was discovered, researchers set out to rationalize the drivers behind this relationship with an analysis of the thermodynamics involved in both UPD and bulk metal reduction. Sudha et al. outlined the steps as (i) moving metal ions from the bulk to the reaction zone, (ii) removing the solvation shell, (iii) electron transfer from the substrate to the metal ions, (iv) removal of solvent dipoles from the substrate, and (v) bond formation between the metal and the substrate. This more rigorous analysis illuminated the true complexity in predicting ΔU_p, and terms such as the lattice coordination number of the substrate and metal, degree of substrate coverage, solvent desorption energies, and enthalpies of bond formations were integrated into a more dependable model. Furthermore, examination of step (iii) highlighted that the Gibbs free energy change of transferring electrons from the substrate to metal ions in the reaction zone depends on the work function of the substrate. [32] [33] Therefore, the difference in potential between reducing a metal onto a foreign substrate and reducing onto the same substance (i.e. bulk reduction) is directly dependent on the difference in work functions of the two substrates. This information aids in the process of materials selection when UPD is desired by giving an indication for which material pairs will work well together for this process. The selection

of substrates with high work functions and depositing metals with low work functions permits for formation of a metal thin film limited to just one ML, when potential is properly controlled.

The limited growth of the sacrificial metal, thanks to the difference in work functions between the adlayer and substrate, then templates and limits the deposition of a more noble metal during the electroless replacement step. Furthermore, because SLRR is solution based, carried out at low temperatures, and generally minimizes excess energy, the noble metal films can avoid ripening and conform to unique support geometries. Advances in this process include the development of electrochemical cells where the electrolyte can flow through for easier switching between steps [34] and a one-cell configuration that simply incorporates ions of the sacrificial metal and the more noble metal in the same electrolyte. [35]

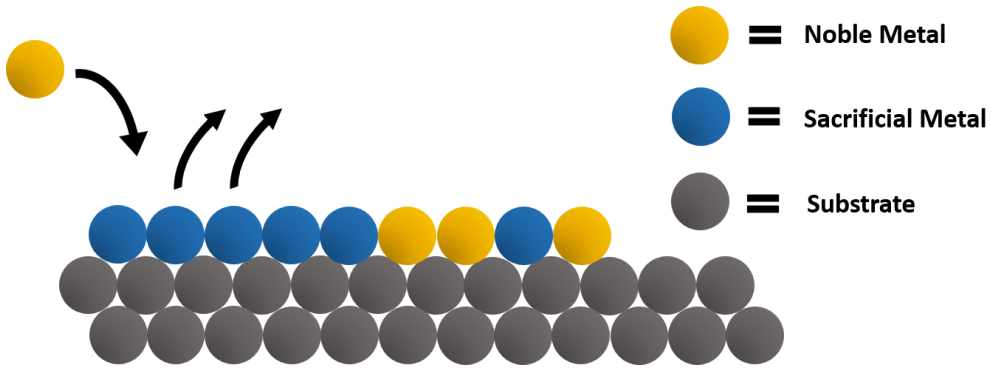

Figure 1.3 – This schematic displays the SLRR process of depositing a sacrificial metal on the surface of the substrate and subsequent replacement of that sacrificial layer with a more noble metal.

1.5 Research Objectives

The objectives of this work are to investigate the prospect of depositing Pt-ML on two unique substrates that have the potential to advance the development of electrocatalysts and our understanding of interface interactions between precious metals and their supports. The strategy in both cases involves utilizing SLRR, a solution-based, electrochemical, process for deriving atomically thin precious metal films. As indicated above, this technique has been highly successful throughout the past decade for achieving precision, wetted film growth on 2D substrates.

In Chapter 2, 3D graphene grown on an open-celled Ni foam was used as a support for the fabrication of Pt-ML. Interest in this catalyst support resonates because of its potential for scaling the synthesis of precious metal nanostructures while tuning catalytic activity through interface interaction with graphene and metal-ligand effect from Ni. Furthermore, the ability to remove the interior Ni frame via etching allows for the option of incorporating a ligand effect of ones choosing, tailoring the electronic properties of the Pt-ML.

Then in chapter 3, a MoS2 thin film of varying thickness is used as the substrate for Pt deposition. By varying the substrate thickness between 1 nm and 30 nm it is possible to observe the manner in which Pt decorates the surface of the MoS_2 as a function of the concentration of available MoS_2 edge sites. This is because MoS_2 can change orientations between one where the basal plane is parallel to the substrate to one where the basal plane becomes perpendicular to it. Additionally, altering the quantity of Pt deposited, allows for observation of the influence of MoS_2 on the electronic properties of the deposited Pt. The

objective here is gain a better understanding of the catalyst and support interactions between MoS_2 and Pt.

CHAPTER 2. SYNTHESIS OF PLATINUM MONOLAYERS ON GRAPHENATED 3D NICKEL FOAMS

2.1 Introduction

As discussed in Chapter 1, lower material costs and increased catalytic activity via ultra-low loading of precious metals remains significant area of catalyst research. Even though the standard for many commercial catalyst applications remains Pt nanoparticles on a carbon black substrate, cutting edge research has moved on to create novel nanomaterial structures such as core-shell and layered catalysts. These structures combine pseudomorphic overlayers of precious metal and cheaper transition metal interiors that may lower material costs while enhancing catalytic activity. [36] For these multicomponent catalysts, selection of the underlying material becomes important since the substrate can influence catalyst activity, selectivity, and durability when the catalyst overlayers remain atomically thin. This occurs via phenomena such as the metal ligand effect and lattice strain mentioned in Chapter 1. [37] [38] Catalysts incorporating these innovative ideas can significantly outperform commercial catalysts, but most studies remain fundamental, taking place at the nanoscale, with no proposal for scaling the technology to widespread adoption. For this reason, new processing techniques are required to bring these state-of-the-art catalysts to the macro-scale without sacrificing performance.

A novel concept for accomplishing this goal came out of a collaboration with Dr. Jamie Warner's group at the University of Oxford. They have been working with a variety of 2D materials and emphasizing their incorporation into nanoscale heterostructures for

studying the unique properties that arise. Recently this involved CVD grown graphene on an open-celled Ni foam, a process that resulted in a multilayer graphene, as discussed within this chapter. The graphenated Ni foam presented an interesting opportunity to study the deposition of precious metal on a dramatically different support from those typically worked with in electrocatalyst research. Its novelty arises from the potential for both (i) the application of precious metal nanostructures on a highly scalable substrate and (ii) tuning electronic properties of the precious metal. Moreover, the substrate, possesses appealing qualities such as, relatively low cost, excellent electrical conductivity, and high surface area to volume.

The resulting graphene surface from the CVD process features curvature from the Ni foam and heterogeneities that would certainly influence the deposition of Pt. As I have stated in Chapter 1, studies reveal that graphene containing defects, inclusions, or oxygen based functional groups is able to form strong bonds with precious metals. These sites act as anchor points that bind metal with high affinity, preventing dissolution and encouraging distribution across the surface of the support. However, nucleation can result if metal atoms are unable to diffuse across the surface of the substrate. Therefore, care was taken to deposit Pt in a manner that would avoid agglomeration in individual areas of the macrostructure, and instead achieve optimal atomic film growth, with the ultimate goal of depositing Pt-ML. As discussed, ML growth improves upon nanoparticle overlayers by optimizing the ECSA to mass ratio and encouraging interface interactions between catalytically active material and the support.

SLRR was selected as the best option for synthesis of Pt-ML based on its ability to form a precious metal skin on a variety of surfaces. [39] [26] The thought behind this was

that the self-limiting and solution-based nature of this technique would help overcome the hinderance of attaining highly wetted films on a 3D substrate. SLRR uses potentials less negative than those required for bulk metal reduction, resulting in bond formation between adsorbate and substrate via UPD. This UPD layer then gets replaced by a more noble metal at OCP. This helps encourage ML growth of precious metals, and is especially beneficial when depositing metals that possess higher surface energy. Multiple iterations of this process results in thin films of well controlled thickness and a high degree of surface wetting. [39] [40]

Additionally, my research group's previous work indicates that use of SLRR with a single interlayer graphene between a 2D Au film and Pt overlayers encourages strained Pt lattice growth and improves catalytic performance when compared to samples without graphene. Graphene did not hinder the flat, uniform growth of Pt overlayers, and the substrate was completely masked by just four monolayers of Pt. [26] Observed catalytic enhancement aligned well with findings of others, that Pt lattice compression can improve electrocatalytic performance. [41] [42] [37] These finding helped reinforce the decision for utilizing SLRR to deposit Pt on the graphenated Ni foam sample.

The Ni skeleton was not a minor influence in the decision of utilizing this substrate. I have already discussed the benefits of bimetallic catalysts for achieving improved catalytic activity in Chapter 1. But to briefly reiterate, key catalyst properties such as bond formation between adsorbing reactants and the active catalyst sites can be tuned through incorporation of materials that alter electronic structure by straining the Pt-Pt interatomic spacing [41] [43] and integrating the metal ligand effect. [44] For ORR, incorporation of Ni in Pt catalysts has produced some of the most promising results (Figure 1.2), enhancing

both activity and selectivity. [45] [46] [47] [48] [44] [49] [50] [51] [24] [52] [25] [36] [41] [53]

There are a few weaknesses of bimetallic catalysts that need to be overcome before adopting them into commercial production such as, a loss in catalyst longevity when incorporating less stable metals like Ni, but possibly principal among these weaknesses is their complexity. They typically remain specialty materials limited to laboratory research and small-scale production because producing them on a large-scale with any consistency is very difficult. There are a variety of techniques for preparing alloys, layered assemblies, and core-shell structures, including the use of ultrahigh vacuum (UHV) [24] and selective dissolution of the less noble metal [54], but in this thesis I attempt to provide an uncomplicated method for producing tunable catalysts that could be adopted for macroscale synthesis.

A final benefit from this substrate derives from its potential for the Ni substrate to be etched away before or after the deposition of the Pt. The remaining Pt-GR foam can then be broken into nanostructured flakes with potential for redispersion and adhesion on a substrate of choice. The new substrate chosen to interact with the monolayers of Pt through the graphene lattice, could provide tailored catalytic properties (Figure 2.1). In other words, this concept promises the potential for ligand flexibility. Steps taken here include the following: graphene deposition, Ni etching, Pt-ML deposition, and sonication of Pt-ML/GR in DI water.

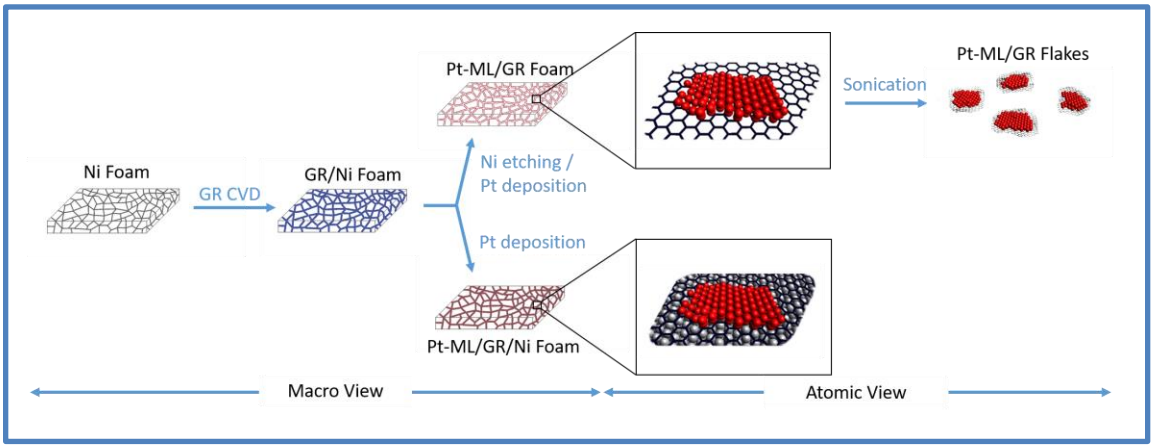

Figure 2.1 - Schematic showing the processing of Ni foams to synthesize 3D Pt-ML on graphene, with and without Ni present as a substrate. Ni-free samples can be further processed to generate flakes of Pt on graphene.

2.2 Experimental

2.2.1 Graphenated Foam Synthesis

A Commercial, open-celled Ni foam was purchased from MTI corporation (346 g/m2 density, ≥ 95% porosity, 80 to 110 pores per inch, 0.25 mm hole diameter, and thickness of 1.6 mm) for use as the initial substrate. Jamie Warner's research group at the University of Oxford used this as a template for precipitation of graphene on the surface. His group shared their graphene growth process, displayed in Figure 2.2. This procedure followed a scheme very similar to that used by Chen et al. [55] An alumina furnace crucible, used as the carrier for the bare nickel foam, was inserted into a 1 inch diameter quartz tube in a horizontal tube furnace. A system with rails was used so that the sample could be rapidly introduced and removed from the hot zone. Before inserting the sample into the hot zone, the system temperature was ramped up at a rate of 50°C/min to a final temperature of

1000°C. As it was heating up, the system was flushed with argon, Ar (200 sccm), hydrogen, H_2 (25% in Ar, 100 sccm) and methane, CH_4 (20% in Ar, 20 sccm). The CH_4 was turned off when the temperature reached around 600°C. Once the furnace temperature was holding constant at 1000°C, the sample was introduced into the hot zone of the furnace. The Ni foam was kept there and annealed for 30 minutes while Ar and H_2 continued to flow. After annealing, CH_4 (20% in Ar, 7 sccm) was introduced for a growth period of 15 minutes (Figure 2.2, blue region). The flow of CH_4 was then shut off and furnace was turned off, allowing it to cool naturally, while the sample was removed from the hot zone. The sample was then removed from the furnace altogether once it had cooled to room temperature. SEM and optical images of the bare Ni and graphenated foam (Figure 2.2(a-c, e)) reveal that the structure is well coated with graphene but otherwise remains unaffected. Higher magnification SEM (Figure 2.2(f)) highlights the presence of inhomogeneities across the graphene surface such as holes and wrinkles.

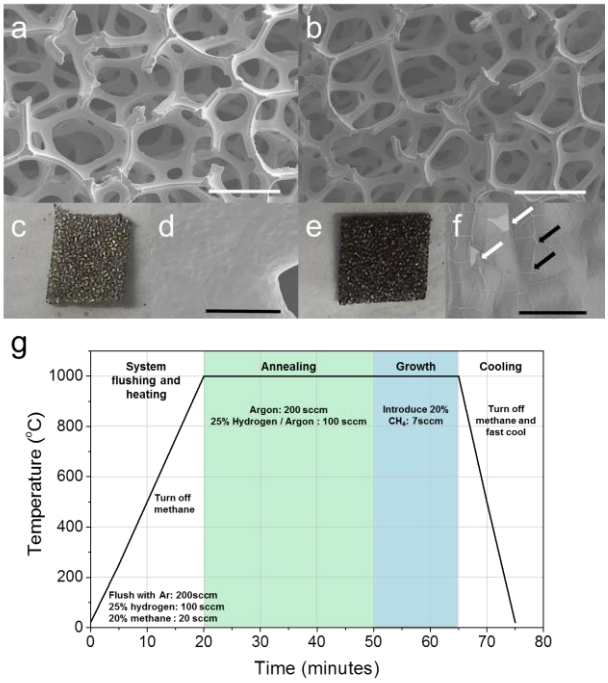

Figure 2.2 - CVD synthesis of graphene on nickel foam. SEM images of nickel foam before (a) and after (b) graphene growth, scale bar 500 µm. c) Optical image of a 1 cm^2 piece of nickel foam and (d) SEM image of the nickel foam surface, 20 µm scale bar. (e) Optical image of a 1 cm^2 piece of nickel foam following graphene growth and (f) SEM image of the graphene on nickel foam with the white arrows indicating holes in the graphene with nickel and the black arrows indicating wrinkles in the graphene, 5 µm scale bar. g) Plot outlining the CVD procedure. (Figure provided by Thomas Samuel as part of his work for Prof. Jamie Warner's research group at the University of Oxford)

2.2.2 Ni Foam Etching

Once the graphene was precipitated on the Ni surface, a free-standing graphene foam was achieved by etching out the Ni skeleton. This process for synthesizing a Ni-free graphene foam was originally outlined Chen et al. [55] The procedure involved first using

a pipette to saturate the GR/Ni foam with PMMA. The sample was then transferred to a furnace and baked at 180°C for approximately 30 minutes. At this point the PMMA cross linking reaction occurred and the PMMA could help maintain the foam structure during the etching process. The PMMA covered foams were then added to a bath of 3 M HCl. The bath was heated to 80°C and the foams were allowed to soak for at least five hours. Foams were periodically flipped to ensure equal etching throughout the sample and the bath was replenished with fresh 3 M HCl as necessary. Based on EDS spot analysis results (Figure 2.4), the etching time of 5+ hours was sufficient to completely remove Ni from the foam. After completing the HCl soak, the foam was lifted out of the acid bath on a glass slide and transferred to a DI water bath for approximately 10 minutes. The foam was then transferred, using a watch glass, to an acetone bath for approximately two hours to remove the PMMA. Fresh acetone was periodically added to keep the bath filled. A shorter soaking time may have worked just was well for removal of PMMA, but two hours was used to try and ensure complete PMMA removal, since any surface contamination could significantly affect Pt deposition. The sample was then transferred once again to DI water to remove residual acetone before being transferred onto the electrode (Figure 2.3). The electrode was produced by wrapping part of a glass slide in conductive carbon tape. Figure 2.5 contains SEM images that highlight the process of depositing graphene on the Ni foam and then subsequent etching. A slight reduction in volume occurred after the etching process. It is somewhat difficult to see in the SEM image (Figure 2.5), but post etching samples have a smaller pore volume.

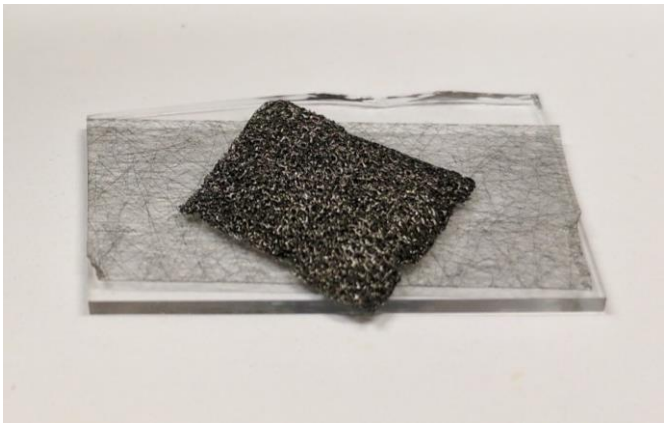

Figure 2.3 – Photograph of free-standing graphene foam placed on the surface of a glass slide coated in conductive carbon tape

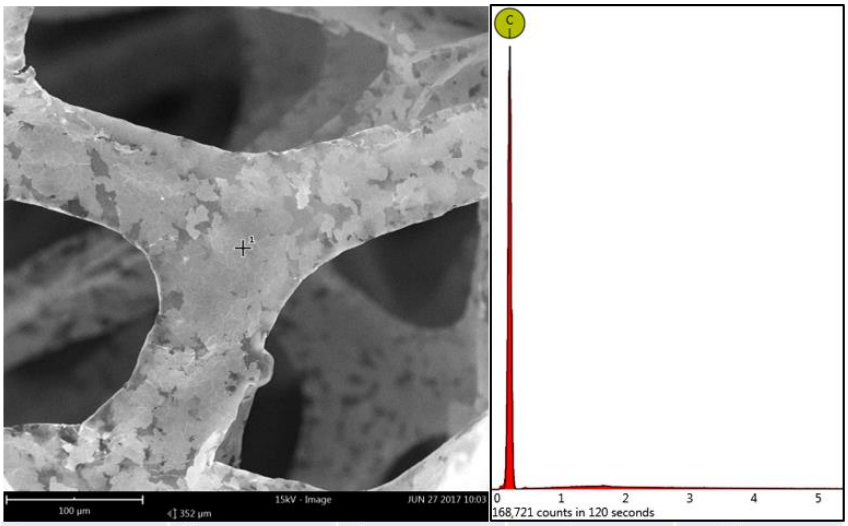

Element Number	Element Symbol	Element Name	Atomic Conc.	Weight Conc.
6	C	Carbon	100.00	100.00

Figure 2.4 – Spot EDX analysis of foam after completing the etching and PMMA removal processes. Accelerating voltage of 15 kV was used.

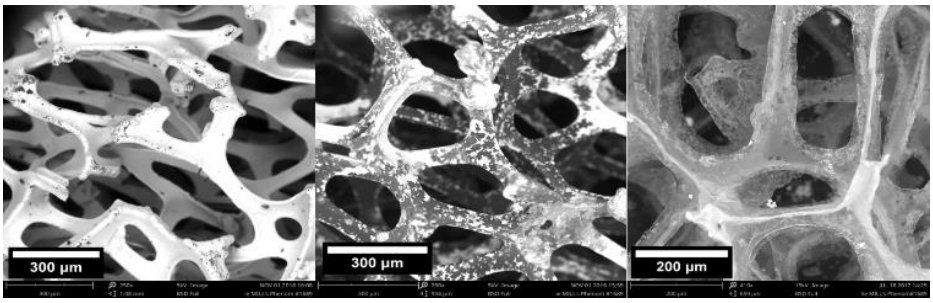

Figure 2.5 - SEM images taken at accelerating voltages of 5 kV and 15 kV with backscatter electron detector. Left image: Open-celled bare Ni foam. Middle image: Graphenated Ni foam. Right image: Etched GR foam

2.2.3 Layer-by-Layer Pt deposition

A Pine WaveNowXV Potentiostat was used for carrying out all electrochemical experiments. Two three-electrode cells (Figure 2.6) were used for the synthesis process. The first cell contained a solution of 10 mM $CuSO_4$ and 50 mM H_2SO_4 and the second contained 0.1 mM chloroplatinic acid. The working electrode was set up in a hanging meniscus configuration in the three-electrode cells. A plug was used to hold the working electrode in place and help maintain the atmosphere inside the cells. Pt wire was used as the counter electrode and Ag/AgCl for the reference electrode. Unless otherwise stated, all potentials are relative to a Ag/AgCl reference electrode. Before beginning the Pt electrodeposition process, ultrahigh purity N_2 was used to purge both solutions for at least 20 minutes. N_2 was flowed over top of the solutions while the cells were in use.

For both sample types (Graphenated Ni foams and Ni-free graphene foams), Pt layers were electrodeposited on the graphene via a method derived from SLRR. First, a few atoms of Cu were put down via bulk electrochemical deposition in cell containing 10 mM $CuSO_4$

+ 50 mM H_2SO_4. The working electrode was then shuttled to the second three-electrode cell, where Cu was replaced by Pt at the open circuit potential (OCP). These first few atoms of Pt would act as seed atoms for additional deposition iterations. Once the initial Pt was put down, Cu UPD could be utilized to continue growth in a more controlled manner. Putting down the initial atoms via bulk deposition was necessary since UPD between Cu and graphene will not occur. This first iteration was the only departure from the typical SLRR methodology. The same procedure was carried out for samples where the Ni had been etched out.

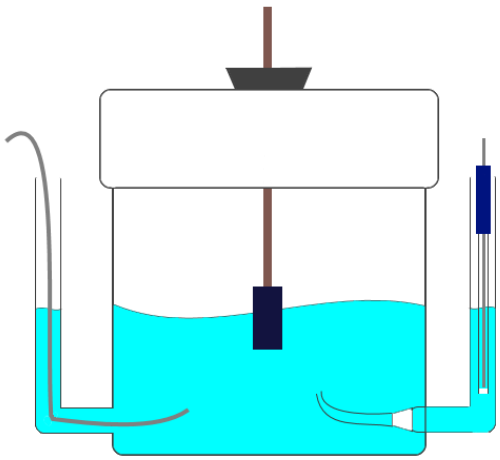

Figure 2.6 – Illustration representation of a three-electrode cell used for carrying out electrochemical experiments

2.2.4 Catalyst Characterization

After Pt deposition, the two types of foam (Graphenated Ni foam and Ni-free graphene foam) were studied to determine the structure of the deposited Pt films and the resulting electrocatalytic characteristics.

2.2.4.1 Structural

To determine the degree of Pt deposition and the organization of Pt atoms on the graphene surface, SEM/EDX (Phenom ProX, 5 kV to 15 kV accelerating voltage), XPS (Thermo K-Alpha, monochromated Al Kα source, selectable spot diameter between 30 and 400 μm), and TEM (FEI Tecnai G2 F30, 300 kV accelerating voltage and Jeol JEM-2200MCO, 80 kV accelerating voltage) were utilized. In imaging samples with the SEM, a backscatter detector was used. TEM characterization carried out on the FEI Tecnai G2 F30 was performed at 300 kV. Samples were prepared by etching out the Ni after Pt had been deposited. For this, Pt/GR/Ni foam was placed in 3M HNO_3 for approximately 3 hours and then lifted out on a glass slide and moved into DI water. The etched foam in DI water was shaken vigorously to disperse flakes of Pt/GR throughout the water. A drop of the solution containing Pt/GR foam flakes was then deposited on holey carbon TEM grids, and the grids were heated to approximately 40°C for 30 minutes to avoid the so called coffee ring effect. The second TEM characterization was performed on a Joel JEM-2200MCO at an accelerating voltage of 80 kV. Samples for this session were prepared using the etching process outlined in section 2.2.2 followed by the Pt deposition process discussed in section 2.2.3. The Pt/GR/Ni foam was then rubbed onto a holey carbon TEM grid.

2.2.4.2 Electrochemical

Characterized of the Pt films deposited on Pt/GR/Ni and Pt/GR foams also involved the use of CV and LSV in a three-electrode cell (Figure 2.6). The cell was filled with an electrolyte of 0.1 M H_2SO_4 solution. The working electrode was configured in a hanging meniscus style setup with a catalyst foam attached and completely submerged in the electrolyte. Pt wire was used as the counter electrode and Ag/AgCl was used as the reference electrode. The electrolyte was purged with ultrapure N_2 for at least 20 minutes in an attempted to eliminate any O_2 in solution before running CV and LSV. It was flowed over top while carrying out the experiments. Before recording CV results, the catalyst went through a break in period. This consisted on performing at least 20 cycles of CV at a sweep rate of 50 mV/s. LSV was performed subsequently between the potentials of 1.0 and 0 V (vs Ag/AgCl) at a sweep rate of 20 mV/s. O_2 was then bubbled through the electrolyte before performing LSV for a second time with the same operating parameters. The point of deviation between the LSV data collected with and without dissolved O_2 present was used as the ORR onset potential. The durability study was carried out by cycling the potential applied to the working electrode at a sweep rate of 20 mV/s, between 0.4 and 0.75 V (vs Ag/AgCl). The electrochemical cell was filled with 0.1 M H_2SO_4 and purged with N_2. During cycling, N_2 was directed so that it flowed over top of the electrolyte. The degree of degradation was determined by comparing the integrated area of the Pt reduction peak between the potentials of 0.81 V and 0.20 V (vs Ag/AgCl). The Pt reduction peak was measured using CV at intervals of 0, 500, and 1000 cycles of durability testing.

2.3 Results and Discussion

Raman spectroscopy, HR-TEM, and SEM were used to first study the graphene precipitated on the Ni foam surface. This characterization of the graphene and the resulting figures were produced by Dr. Jamie Warner's research group at the University of Oxford, and I will be discussing them as they relate to this thesis work. Based on RAMAN and HR-TEM characterizations (Figure 2.7 and Figure 2.8), the graphene CVD process produced multilayer graphene approximately 5.5 layers thick on average. TEM was carried out on graphene samples following etching of the Ni skeleton with hot HCl. By observing folds in the graphene, the number of layers was clearly visible and could be counted. Data collected from this process was used to produce a histogram (Figure 2.7(vii)) representing the frequencies of specific layer thicknesses. Figure 2.7(i-vi) displays representations of graphene thicknesses ranging from 1 layer to >10 layers. From these images it is even possible to get an accurate measurement of the spacing between graphene layers (Figure 2.7(ii)). The histogram reveals an average graphene thickness of 5.5 layers with most areas thinner than 13 layers. It is also clear that the most probable thickness was between 3 and 4 layers. This is a good indication that the underlying Ni skeleton and Pt, later deposited on the graphene surface, was separated by approximately 1 nm of graphene in most areas of the foam.

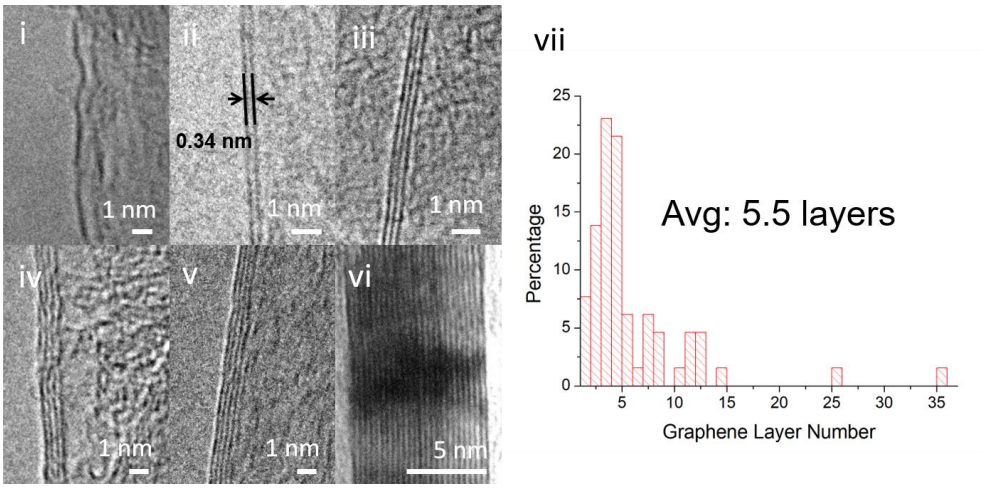

Figure 2.7 - (i-vi) TEM images of folds in graphene foam showing regions of monolayer, bilayer, trilayer, four layer, five layer, and >10 layer graphene. (ii) The interlayer spacing of graphene is indicated. (vii) A histogram gives the distribution of graphene layers determined using folds seen in TEM images. (Figure provided by Thomas Samuel as part of his work for Dr. Jamie Warner's research group at the University of Oxford)

In addition to the TEM work, Raman characterization was carried out on unetched GR/Ni foam (Figure 2.8(a)). Examples of the data collected from the foam are displayed in Figure 2.8(e-g). The ratio of intensities (I_{2D}/I_G) in Figure 2.8(e), being greater than one, is likely from a bi-layer region of graphene. Figure 2.8(f) shows a peak ratio that is expected of a region between 3 and 5 layers thick, and Figure 2.8(g), which shows one of the lowest ratios recorded from these foams, is likely from a graphene region thicker than 5 layers. Above 5 layers, graphene becomes indistinguishable from graphite. Figure 2.8(f) provides an example of a typical D peak, which represents the presence of defects in the graphene. [56] Figure 2.8(b) reveals both the thickness of the graphene layers and the presence or absence of defects in selected regions of the foam. The blue dots marking the foam in

Figure 2.8(a) display the regions sampled, with positions 1-7 representing different regions of the tube furnace during graphene growth. Positions 1 and 7 were closer the furnace ends, whereas position 4 was close to the center. These same positions were sampled on the top and bottom of foams. Observed variance in the ratio of 2D to G Raman peaks was always within experimental error (Figure 2.8(b)) suggesting that the number of graphene layers is independent of position. A 2D/G ratio of less than one, which was observed across the entire foam sample, is indicative of multi-layer graphene. This is expected for graphene formed on Ni via CVD. [57] Lack of variation in the D to G peak ratio (Figure 2.8(b), black line) indicates that the graphene formed is relatively defect free and high quality. Comparison of the top, bottom, middle, and edges of the foam samples (Figure 2.8(c)), suggests that more defects are present at the bottom and edges, although the D peak only appeared in a small number of the recorded spectra. Even though analysis of this data leads to a similar conclusion as TEM on the number of graphene layers present, it should be noted that the error bars on the thickness data shown here are quite large. Therefore, the TEM characterization and resulting histogram should be considered a more reliable representation of the number of graphene layers throughout these samples.

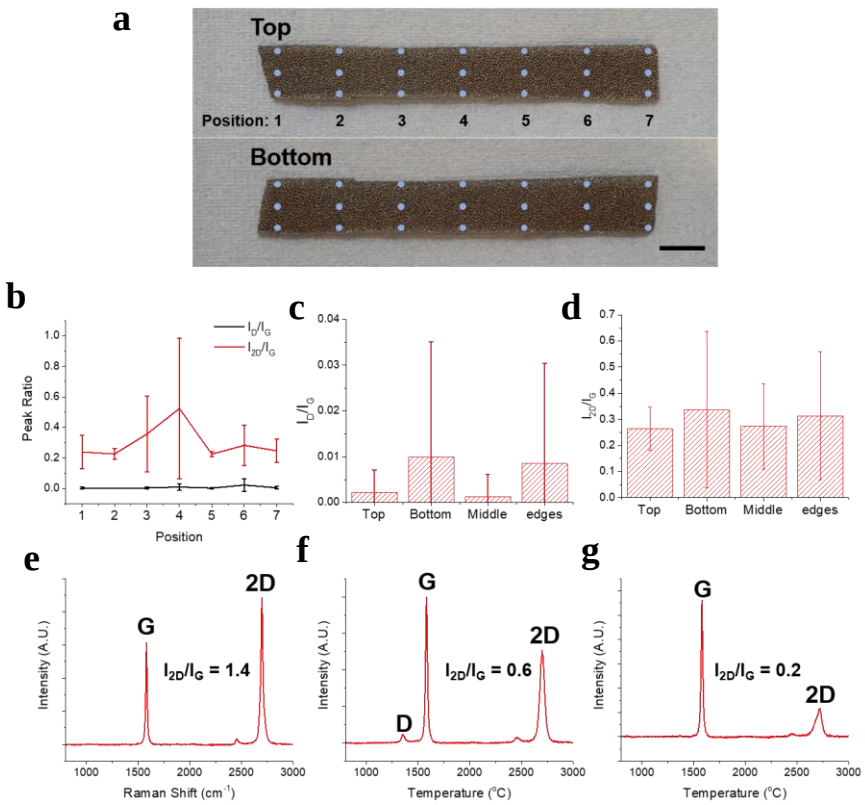

Figure 2.8 - Raman characterization of large pieces of CVD graphene foam on nickel. (a) Image of graphene foam pre-etching, each blue spot corresponds to a location where Raman spectra were recorded, 1 cm scale bar. (b) Raman D/G and 2D/G ratios as a function of the positions indicated in (a). Position dependent (c) D/G and (d) 2D/G Raman peak ratios. (e) Raman spectrum indicating the presence of bilayer graphene. (f) Raman spectrum with D peak indicating the presence of defects. The 2D/G ratio indicates graphene with fewer than 5 layers. (g) Raman spectrum indicating graphene with a thickness of >5 layers. (Figure provided by Thomas Samuel as part of his work for Prof. Jamie Warner's research group at the University of Oxford)

While an SEM characterization is less useful here for determining the number of graphene layers, it can provide key insights into the structure of the foam on a mesoscale. Figure 2.9 shows SEM images taken of graphene foam after etching of the Ni skeleton, at

an accelerating voltage of 3 kV. Figure 2.9(i-iv) are shown in order of increasing resolution. It is interesting to note that the graphene is well interconnected throughout the foam, with very few complete breaks visible, even after a harsh etching process. Figure 2.9(iii) indicates the presence of holes along the length of a given graphene branch but these do not seem to hamper retention of the Ni skeleton structure. This is seemingly a benefit of thicker graphene that grows on Ni substrates. The same process for creating free-standing graphene foam would likely not work with a Cu skeleton without collapse of the structure. [55] The graphene also appears smooth across the surface but with apparent changes in thickness and wrinkles indicated by changes in contrast. Figure 2.9(iv) displays the efficacy of the Ni etching process in creating hollow graphene branches.

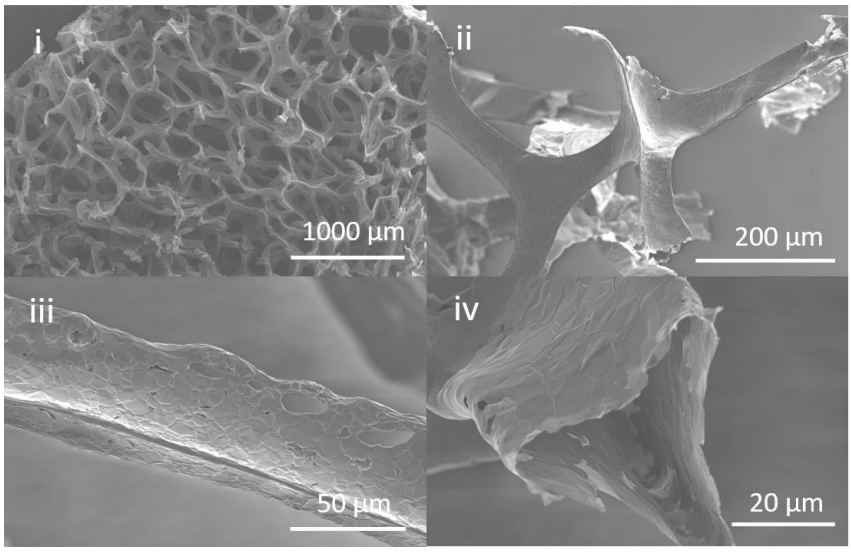

Figure 2.9 - SEM images of etched graphene branches with increasing degrees of magnification. (iii) SEM image of a graphene branch showing the presence of multiple holes. (iv) Image showing the hollow nature of the graphene foam. (Figure provided by Thomas Samuel as part of his work for Prof. Jamie Warner's research group at the University of Oxford)

After receiving the graphenated Ni foams from Dr. Jamie Warner's lab, Pt was deposited on the graphene surface of both samples with Ni intact and those that had undergone the etching process outlined in the Experimental section. As mentioned, I adopted a derivative of SLRR in an attempt to deposit precious metal ML on a graphene surface. Typical SLRR, involving Cu as the sacrificial metal, results in a partial monolayer deposition with each iteration. This is because every Pt(IV) atom deposited results in the oxidation of 2 copper atoms that enter the solution as Cu(II). [26] [35] Because of this level of precision, the amount of Pt deposited on a given sample can be well controlled and minimized. This is ideal for precious metal catalysts, which require minimal loading to lower costs. SLRR also results in Pt deposition with minimum energy expense. Therefore, the Pt can avoid ripening and grow in more epitaxial manner, and approach the theoretical maximum number of electrochemically active surface sites for the mass of Pt. The technique used in this thesis is similar in the sense that Pt(IV) is getting reduced and Cu is getting oxidized to Cu(II), but differs in the quantity of Pt deposited with each iteration, at least initially. Because Cu does not UPD on the graphene surface, a primary monolayer must be put down before this technique exactly emulates typical SLRR.

TEM characterization was performed on samples after completing several iterations of Pt deposition. In examining a Ni-free sample with an aberration corrected microscope at an accelerating voltage of 80 kV, it was found that Pt was arranging in many areas of the graphene surface in the form of a square lattice (Figure 2.10(b)). Interestingly, this type of lattice growth appears to show {100} Pt instead of the energetically preferred {111} growth. Previous work by our research group presented the possibility of a compressed Pt lattice on a 2D graphene substrate through use of EXAFS, suggesting that graphene is able

to template Pt growth via strong bond formation between graphene and Pt. [26] Then in a follow-up study, HR-TEM characterization of Pt-ML on Au-film with a interlayer of single-layer graphene identified epitaxial Pt growth on the graphene surface. Careful analysis of the HR-TEM images showed that between one and two ML of Pt was present across the surface of the graphene and that Pt atoms were depositing at every other C-C bond in the zigzag direction and at every C-C bond in the armchair direction, encouraging {100} Pt lattice growth. [58] Therefore, from what appears to be the same structure in the case of 3D graphene sample, provides strong evidence that Pt is being deposited in templated layers on the graphene surface despite the substrate's unusual geometry. Figure 2.10(b) also appears to show some contrast variation across the surface of the Pt growth area. This indicates that {100} Pt lattice growth is being templated beyond the first layer of atoms and extends into at least one or two additional Pt layers.

Pt-ML growth that is perhaps compressed is meaningful because (i) lattice compression has been shown to improve electrocatalytic performance for ORR [43] and (ii) ML growth indicates that Pt is getting deposited in a manner that maximizes its interaction with the substrate and its total number of available reaction sites. Observation of this growth type on an uncontrolled, 3D surface reinforces the possibility that electrocatalytic enhancement can be preserved on a scalable surface. That is, samples with much larger geometric surface areas could be produced in a similar manner with Pt growth that mirrors that which we have achieved. This is critical since 2D substrates severely limit the extent of catalytic surface produced, whereas 3D substrates could greatly increase that limit.

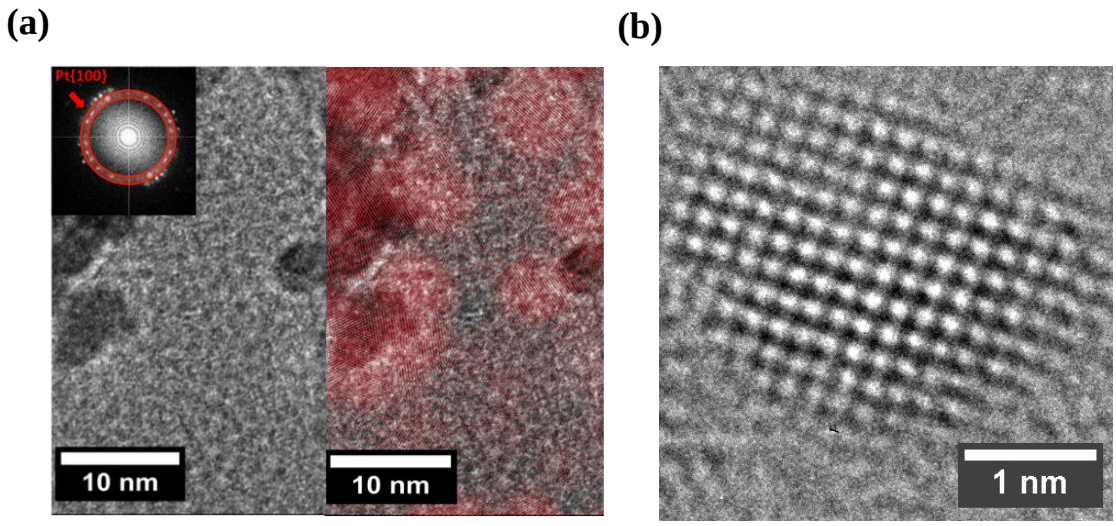

Figure 2.10 – Characterization of Pt-ML/GR foam with TEM. (a-left) BF TEM image of etched Pt-ML/GR foam with inset displaying FFT with polycrystalline Pt{100} spots indicated. (a-right) composite image of BF TEM image and IFFT of Pt spots with Pt areas highlighted in red. (b) BF, High-resolution TEM image of square Pt lattice, 80 kV accelerating voltage

A similar TEM characterization was performed on a sample of Pt deposited on graphenated Ni with a 300 kV accelerating voltage. The voltage proved to be too energetic for observation of the few layers of graphene present, but regions containing Pt could be easily identified. In the left frame of Figure 2.10(a) a Pt-rich region is displayed. The inset displays a FFT produced from this image with a red ring highlighting spots from the Pt{100} crystal plane. Using these spots, an IFFT was then produced and superimposed over the original TEM image to form a composite. This image is displayed in the right panel of Figure 2.10 with the Pt regions tinted red to provide contrast. What stands out, aside from the Pt nanoparticles decorating the edges of the images, are the areas of Pt being indicated between those nanoparticles. If present in these areas, Pt would exist as films no

thicker than the C mesh substrate. This evidence reinforces the idea that Pt is going down as ML in some region of the graphenated surface.

After reviewing promising data from the TEM images, it was important to understand the extent of Pt coverage across the surface of the catalyst support. For this purpose, EDX mapping was used (Figure 2.11). In an attempt to gain more surface sensitivity with this technique, 5 kV was used for the accelerating voltage. With the Ni skeleton intact, as is the case here, the strongest signals come from the Ni and the graphene overlayer. However, a weaker signal from the Pt can still be detected. With the resolution of this SEM, it is impossible to determine the type of Pt growth present, but the x-ray detector was sensitive enough to show characteristic x-rays from the M absorption edges of Pt. In this relatively uniform looking region of graphene capped Ni, EDX results suggest that Pt is well dispersed across the surface. This result is promising, as it suggests that Pt is well distributed throughout the foam sample, increasing the potential for scalability of this process. It should be noted that Pt appears to also be covering the areas where no graphene is present. It is thought that the Pt will readily replace exposed Ni along with Cu during the electroless replacement phase of the deposition process. A more uniform graphene layer on the Ni substrate would likely avoid this since graphene prevents diffusion of metallic species in applications such as corrosion resistance. [59]

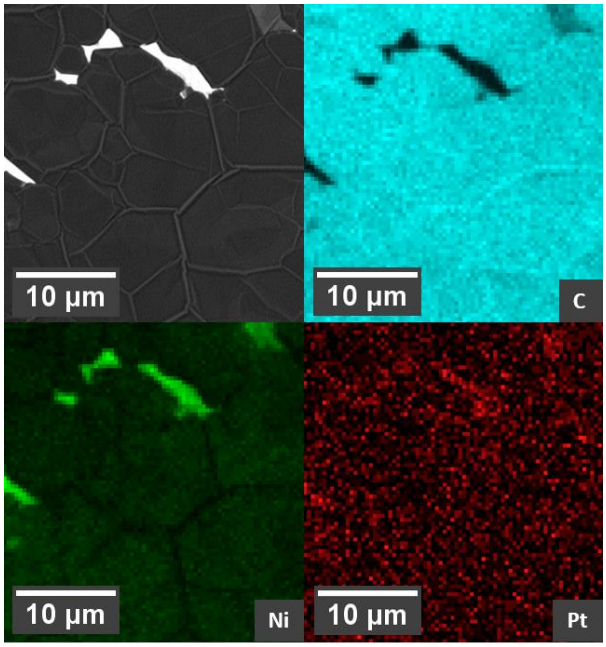

Figure 2.11 - Characterization of Pt-ML/GR/Ni foams with SEM/EDX. SEM image of a foam branch with EDX spectra of C, Ni, and Pt.

To determine the chemical state of the surface Pt, XPS scans were performed on the platinized foams with and without Ni present. The x-ray source was Al Kα and a Pt foil reference sample was used. Based on high-resolution scans of the Pt4f doublet (Figure 2.12), it appears that Pt exists in a metallic state for both sample types. This is somewhat expected for Pt in the presence of Ni, since the Ni will oxidize readily compared to Pt. The peak positions, indicated with dashed red lines, shows no discernable shift in the $Pt4f_{7/2}$ and $Pt4f_{5/2}$, indicating no significant impact on the Pt core level electrons. This is interesting because of the impact that Ni is expected to lower the Pt d-band center via charge transfer. [24] However, other groups such as Mintsouli et al. observed the same phenomenon in the fabrication of Pt/Ni core shell structures on high surface area carbon

supports. [60] Groups reporting XPS results from Pt on Au substrates also found that above 2 ML, Pt becomes less cationic and begins to order similarly to bulk Pt. [38] High resolution scans were also performed for the Ni $2p_{3/2}$ and $2p_{1/2}$ peaks on etched and unetched samples (Figure 2.12). The blue line representing the sample with Ni removed, helps to conclude that the Ni etching process is highly effective. Because XPS is such surface sensitive technique, any residual Ni should be easily detected. The sample with Ni foam intact prior to Pt deposition is represented by the black line. Based on the Ni 2p peak positions of the sample containing Ni, it appears that Ni exists in an oxidized state. This is likely the state of Ni right at the interface between graphene and Ni since XPS is likely to only probe the first layer or two of Ni.

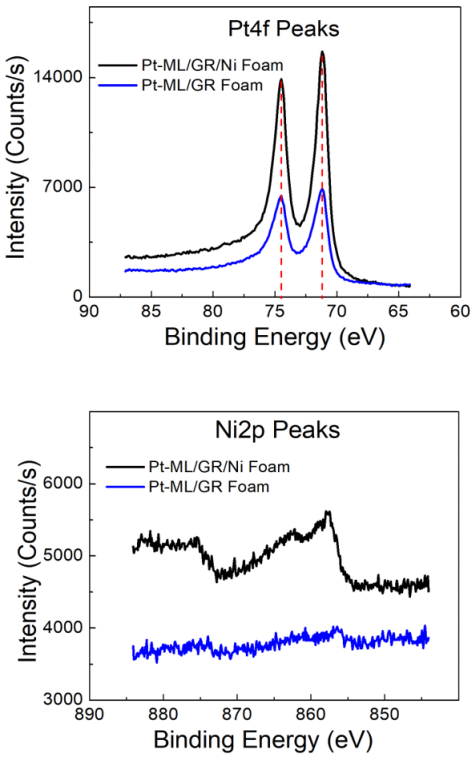

Figure 2.12 - XPS characterization and electrocatalytic performance of Pt-ML foams and commercial Pt/C catalyst. Upper plot showing Pt 4f7/2 and 4f5/2 doublet from Pt-ML/GR/Ni and Pt-ML/GR foam samples. Lower plot displaying Ni 2p3/2 and 2p1/2 doublet with satellite features from Pt-ML/GR/Ni foam sample and lack of Ni2p peaks from Pt-ML/GR foam sample

Electrochemical characterization of the synthesized samples started with performing CV. Potential was swept between -0.3 V to 1.2 V at a rate of 50 mV/s. Integration of the hydrogen UPD region of the CV curve provides an estimate of the ECSA. This is because hydrogen reduction is a one electron transfer reaction and only one hydrogen can adsorb to each Pt atom for UPD. Therefore, total charge transfer can be easily related to the total number of Pt atoms at the catalyst surface. Then, by assuming the standard packing fraction

for the Pt lattice, the ECSA can be estimated. The same result can be obtained by integrating the Pt reduction peak, but using the hydrogen UPD region for ECSA estimates has become standard practice. Figure 2.15 contains the voltammogram from a typical Pt-ML/GR/Ni sample. The figure shows a clear Pt reduction signal at approximately 0.4 V (vs Ag/AgCl), but the oxidation signal is a bit more difficult to pick out. This is partially because of the naturally elongated Pt oxidation peak, but it also gets somewhat masked by the presence of a Ni oxidation feature and the onset of O_2 evolution. It is unexpected that a Ni oxidation signal remains after the extended break-in period performed prior to recording this voltammogram, since exposed Ni atoms usually dissolve readily in an acidic solution. One possible explanation for this is that Ni oxides are able to form but graphene prevents dissolution, indicating the prospect of improved catalyst longevity. However, to make any meaningful conclusions about the longevity of these catalysts, durability testing was needed.

Some early durability testing was performed on one of the original iterations in the development of the Pt-ML/GR/Ni foam catalyst. The testing consisted of cycling the applied potential to the working electrode between 0.4 and 0.75 V (vs Ag/AgCl) in an electrochemical cell containing 0.1 M H_2SO_4, that had been purged with N_2. Then, at intervals of 0, 500, and 1000 cycles, CV was performed. This allowed for comparing the integrated area of the Pt reduction peak to assess the degree of catalyst degradation at each interval (Figure 2.13). The comparison revealed that after 1000 cycles approximately 80% of the ECSA remained. The causes of degradation are unknown from this initial assessment but could include agglomeration of Pt nanostructures, dissolution of Pt, or dissolution of Pt supports that resulted in loss of Pt as well. The 80% reduction in ECSA is in line with

previous work by our research group that compared the durability of Pt-ML catalysts synthesized on a Au film substrate, with and without a single layer of graphene present between the Pt and Au. It found that Pt films at or above three ML in thickness, retained approximately 73% of the original ECSA after 1000 cycles (Figure 2.14). It is encouraging that the foam samples show similar robustness, but it is worth noting that durability testing in our group's previous study bubbled O_2 through the electrolyte instead of N_2. The presence of O_2 is likely to have a negative impact on catalyst durability and should be considered when comparing results. Follow-up durability tests with a greater number of cycles should still be performed to get a better idea of the true longevity of the foam catalysts. Additionally, using a more recent iteration in the development of the foam catalysts would give more meaningful information, since it would more accurately represent the desired catalyst structure.

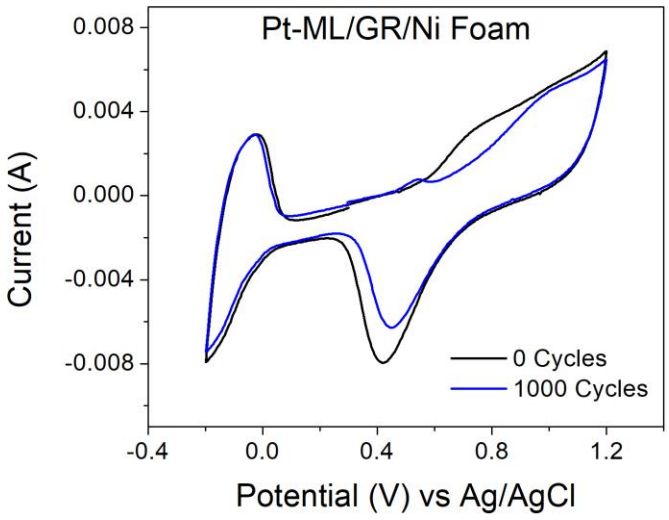

Figure 2.13 - CV plots from a Pt-ML/GR/Ni sample before beginning durability testing and after 1000 cycles of durability testing. The Pt reduction peak at ~0.45 V (vs Ag/AgCl) was used in determining the amount of ECSA.

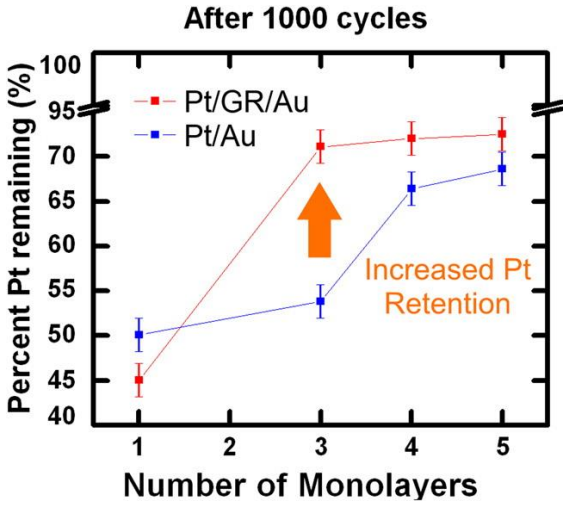

Figure 2.14 - Using the Pt reduction shape in CV, the percentage of surface Pt is calculated after 1000 cycles in acidic media. Cycles were performed from 0.4 to 0.75 V in O2-saturated H2SO4 (Reprinted with permission from [26]. Copyright 2015 American Chemical Society)

Additional electrochemical evaluation was performed to determine the electrocatalytic performance of the fabricated catalysts, in terms of the ORR overpotential. This consisted of performing LSV between the potentials of 1.0 and 0 V (vs Ag/AgCl) at a sweep rate of 20 mV/s. The onset potential was determined by performing this experiment with and without O_2 present in solution and then finding the point of deviation between the two data sets (Figure 2.15). Typically, this kind of catalyst evaluation is performed on a rotating disk electrode to mitigate any mass transfer effects, but the size and geometry of the foam catalyst made the use of a rotating disk electrode prohibitive. Instead the working electrode was stationary in a hanging meniscus configuration for this testing. For comparison a commercial Pt/C catalyst was also prepared. This consisted of mixing 46.1% Pt/C with D.I. water, IPA, and Nafion, followed by an ultrasonic bath to disperse the catalyst before drop casting onto a glassy carbon electrode. Comparison of the onset

potentials (Figure 2.16) indicates that samples containing Ni outperformed the Pt-ML/GR foam and commercial catalyst by approximately 87 mV. The Pt-ML/GR electrode performed comparably to commercial Pt/C. Each of the three electrodes outperformed a 2D Pt-GR-Au electrode used in previous, similar experiments in this lab, (Figure 2.16) and used here as a basis for comparison. Viewed holistically, results indicate that Pt lattice strain due to the graphene substrate, although implied by the TEM analysis, did not improve electrode performance substantially relative to that of the Pt commercial product. When Ni remained part of the substrate, significant improvement (reduction in overpotential for O_2 reduction) was preserved in the 3D catalyst, presumably due to the trans-graphene, Ni-ligand effect on Pt performance.

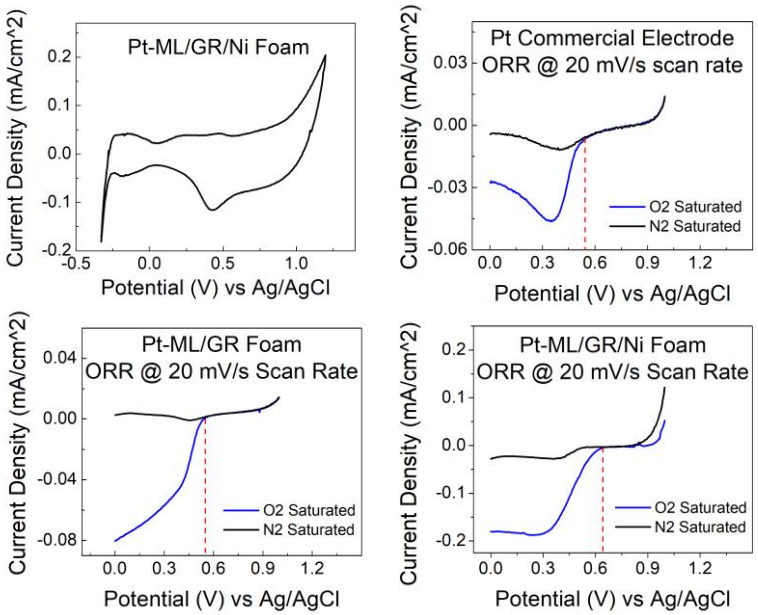

Figure 2.15 - CV of typical Pt-ML/GR/Ni sample with scan rate of 50 mV/s and LSV plots indicating ORR onset potential for Pt-ML/GR/Ni foam, Pt-ML/GR foam, and commercial Pt/C catalyst.

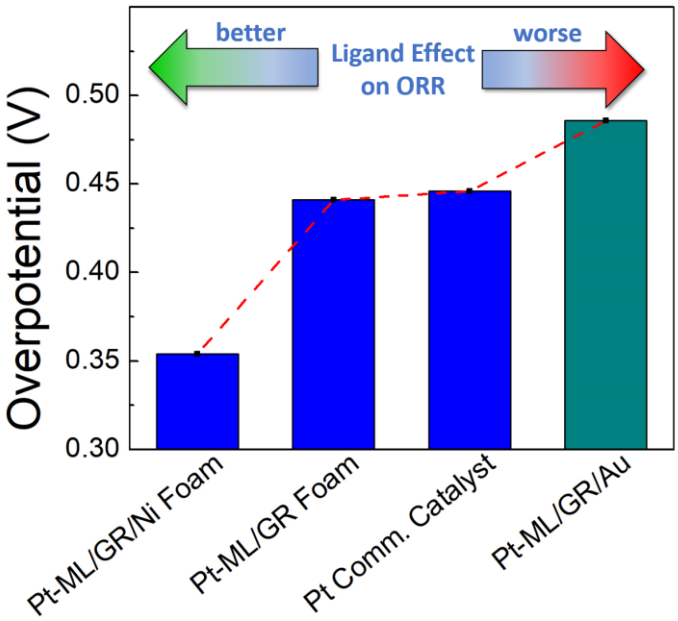

Figure 2.16 - Comparison of ORR overpotentials for foam catalysts and commercial Pt/C catalyst

The role of Ni and other transition metals in enhancing the activity of Pt is an extensively explored area of research. The boost in catalytic performance we observe here is important since graphene is electronically transparent in the sense that it does not seem to discourage the Ni ligand effect, even in the 3D electrode environment created for these experiments. In addition, by introducing a graphene sandwich layer, we have essentially decoupled the phenomena of a strained, 2D Pt lattice and the ligand effect, which are typically co-induced by a single type of substrate. This last concept is promising for applications where it is desirable to have interchangeable ligand effects, since we should be able to harvest the Pt nanostructures from the Ni skeleton and disperse them as Pt-ML/GR onto a new substrate. Work necessary to confirm the latter concept (substrate substitution) lies outside the scope of this thesis.

2.4 Summary

These results strongly indicate that we have developed a method for producing an enhanced, Pt-lean catalyst in a macro arrangement. The non-uniform graphene interlayer templates the Pt deposition and remains sufficiently thin enough in most areas for electronic transparency essential to positive Ni-Pt interactions. In combination with ultrathin Pt growth, this encourages the substrate to play a role in electrocatalytic properties, boosting ORR performance. Furthermore, the highly porous, graphene-capped Ni foam substrate combined with low temperature electrochemical deposition has huge potential in terms of scalability and versatility of structure. Our findings also suggest, that Pt-ML/GR can be decoupled from Ni and be applied to additional substrates, providing catalysts with electronic properties tailored to the application.

CHAPTER 3. SYNTHESIS OF PLATINUM MONOLAYERS ON MOLYBDENUM DISULFIDE THIN FILMS

3.1 Introduction

MoS_2 is considered a 2D material, although each MoS_2 layer is approximately 6.5 Å thick and consists of a layer of Mo sandwiched, via covalent bonds, between two layers of S atoms. Layers of MoS_2 then interact with one another via relatively weak van der Waals forces. One of the most significant differences between this material and the most famous 2D material, graphene, is its bandgap of ~1.8 eV for single layer and ~1.2 eV for multilayer. The meeting of the valence and conduction band at Dirac points make graphene a zero-gap material and an excellent conductor, but this property is a weakness for applications such as optoelectronics and transistors where some bandgap is required. Therefore, MoS_2 has garnered attention as a 2D material in the area of microelectronics. Even still, MoS_2 is rarely used on its own, but rather gets hybridized with other materials which are generally better for electron mobility.

MoS_2 has also received significant attention in the area of catalysis. For HER, MoS_2 is able to perform competitively with precious metal catalysts at low overpotentials. Despite this, Pt remains the most popular catalyst for this reaction with little room for improvement in terms of activity. Other groups have found MoS_2 to be a valuable substrate, reporting the benefits of its high surface area, chemical inertness, and ability to modify electronic properties of precious metal nanoparticles. For Patil et al., this concept yielded a catalyst that outperformed commercial Pt/C for methanol oxidation by avoiding CO

poisoning typical in state-of-the-art industry catalysts. [18] However, even nanoparticles are going to be suboptimal in terms of substrate utilization, ECSA, and adjusting electronic properties via catalyst and support interactions. Ideally, the precious metals such as Pt get arranged in highly wetted thin films that full utilize the available substrate and approach the theoretical maximum ECSA to mass ratio. As mentioned previously, monolayer formation is also beneficial for allowing the substrate to influence electronic properties of the overlayers through strain and the so-called ligand effect.

As discussed in Chapter 1, SLRR is an excellent technique for depositing highly wetted thin films. The challenge of optimizing Pt deposition on an MoS_2 substrate presented another opportunity to explore the versatility of this technique. What sets MoS_2 apart as a substrate for depositing precious metal via SLRR, is the reactivity of its different planes. It is understood that it is the metallic edge sites and not the basal planes that are highly reactive in MoS_2 films. We can therefore assume that this will impact the electrochemical deposition of Pt, especially in this case, where highly wetted monolayers are the objective. To explore this, we produced MoS_2 ranging from 1 nm to 30 nm in thickness. MoS_2 will realign itself depending on the thickness of the Mo seed layer during synthesis, with seed layer films <~3 nm resulting in horizontally aligned MoS_2, and thicker seed layer films resulting in vertically aligned MoS_2. The horizontally aligned MoS_2 has its basal plane aligned with the substrate and the vertically aligned MoS_2 with exposed edge sites (Figure 3.1). [61] [62] This thesis explores the variation in electrochemical deposition of Pt monolayers by varying both the number of available edge sites and thickness of Pt overlayers.

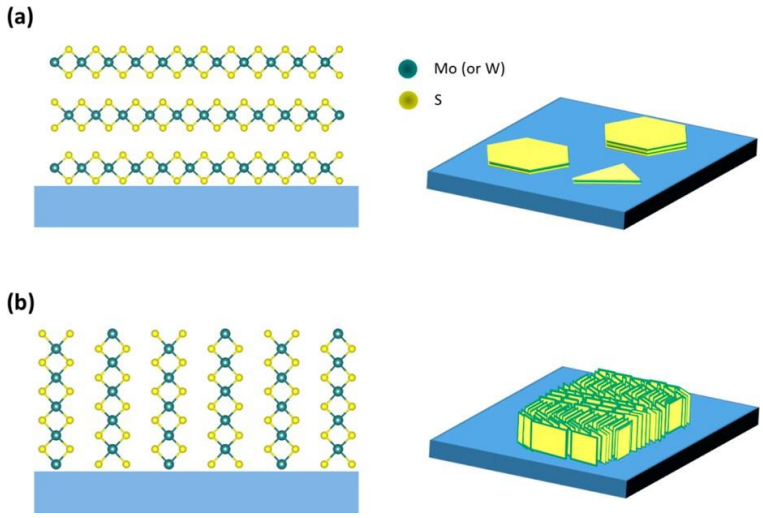

Figure 3.1 – Graphic representation of MoS_2 (a) horizontally aligned and (b) vertically aligned. (Reprinted with permission from [55]. (Copyright 2014 American Chemical Society)

3.2 Experimental

3.2.1 MoS_2 Production

For this work a Ta foil was used as the substrate for the MoS_2 film and the current collector in electrochemical experiments. The synthesis of MoS_2 thin films was performed by Dr. Matthew McDowell's research group, and generally followed the procedure outlined by Kong et al. [63] This involves coating the substrate (Ta foil in this case) with a Mo seed layer through e-beam evaporation. The thickness of the Mo seed layer was varied between 1 nm and 30 nm to produce MoS_2 films of varying thicknesses. Variation in seed layer thickness dictated the orientation of the MoS_2 film, with thinner seed layers leading to horizontally aligned MoS_2 and thicker seed layers yielding vertically aligned MoS_2. After

Mo deposition, a sample was loaded into the center of the tube furnace and S powder was placed at the upstream end. The furnace was pumped down to 100 mTorr and flushed with Ar gas. The furnace temperature was then elevated quickly to 800°C and held at that temperature for 10 minutes. The tube furnace was then turned off and allowed to cool while Ar gas was flowed through. Finally, thermal annealing took place while flowing S gas to prevent film degradation.

3.2.2 Pt Deposition

Electrochemical experiments were carried out using a WaveNowXV potentiostat and three-electrode cells. Pt wire was used as a counter electrode and Ag/AgCl as the reference electrode for all experiments. Initially, it was unknown whether a UPD existed between the sacrificial transition metal ions, Cu(II), and the MoS2 substrate. To explore this, CV was performed in a three-electrode cell containing 10 mM $CuSO_4$ + 50 mM H_2SO_4. (Figure 2.6). This cell was purged with ultrapure N_2 prior to running CV. The potential range was kept between -0.2 and 0.6 V (relative to Ag/AgCl). It was found that potentials more positive than 0.6 V would significantly damage the MoS_2. The working electrode for this experiment was set up by attaching a sample of Ta-MoS2 film to a Cu rod with an alligator clip. Based on the cyclic voltammogram, the onset of bulk deposition starts at ~0.115 V (relative to Ag/AgCl). This was determined by identifying the point where current suddenly became significantly more negative. Additional observation of the voltammogram, showed a small negative current spike just prior to the bulk deposition current. To test whether this spike was a UPD feature, a slightly more positive potential than required for bulk deposition was applied to the working electrode. This test yielded a small amount of current that asymptotically approached zero. This was indicative of deposition being limited to a

monolayer, such as in UPD. Once the onset potential for this UPD between Cu and MoS2 was discovered, it was determined that the target potential for UPD should be set a few mV more negative. This would help ensure formation of a full Cu layer on the substrate surface.

At this point Pt deposition was attempted on a 30 nm MoS_2 sample. The sample, prepared on Ta foil, was first cleaned by running CV in a three-electrode cell containing 0.1 M H_2SO_4 with a lower potential of -0.2 V and an upper potential of 0.6 V (relative to Ag/AgCl). The cell was purged with N_2 for approximately 30 minutes prior to this. The working electrode was then transferred to a three-electrode cell containing 10 mM $CuSO_4$ + 50 mM H_2SO_4 that had also been purged with N_2 for at least 30 minutes. Bulk electrolysis was carried out in this cell at a potential of 0.12 V (relative to Ag/AgCl) for 60 seconds. The working electrode was then transferred to a three-electrode cell containing 0.1 mM chloroplatinic acid that had again been purged with N_2 for at least 30 minutes. OCP was then carried out for five minutes. This completed one iteration of SLRR. The working electrode was then rinsed in DI water and transferred back to the three-electrode cell containing $CuSO_4$ to perform additional iterations. Because Cu(II) and Pt(IV) were used in this process, two Cu atoms get oxidized from the sample for every Pt(IV) atom reduced. Therefore, it was assumed that each iteration deposited 0.5 monolayers. The same process was carried out on all MoS_2 films independent of film thickness.

3.2.3 Characterization

CV and LSV were used to electrochemically characterize Pt-ML/MoS_2 films. Both were carried out in a three-electrode cell filled with 0.1 M H_2SO_4 and purged with N_2 for 30 minutes before running experiments. A lower potential limit of -0.3 V and an upper

limit of 0.6 V (relative to Ag/AgCl) were used along with a sweep rate of 50 mV/s for the CV testing. The upper limit was selected once again to avoid damaging the MoS_2 and the lower limit was selected based on empirical evidence that HER was just beginning to occur. A break in period of at least 20 cycles was performed prior to recording results. For LSV, a sweep rate of 20 mV/s was used along with a starting point of 0.2 V and ending point of -0.8 V (both relative to Ag/AgCl). This range of potentials allowed for the onset and kinetics of the HER to be observed. LSV results from Pt-ML/MoS_2 catalysts were compared with bare MoS_2 and Pt foil.

XPS characterization was carried on Pt-ML/MoS_2 films out using an Al Kα source. Survey scans were performed along with high resolution scans of Pt4f, S2p, Mo3d and Ta4f peaks for each sample. Samples consisted of nine iterations of SLRR on 30 nm MoS_2, three iterations of SLRR on 30 nm MoS_2, and nine iterations of SLRR on 1 nm MoS_2.

3.3 Results and Discussion

3.3.1 Pt Deposition on MoS_2

Each iteration of SLRR for deposition of Pt on MoS2 took place in two-steps. First, bulk electrolysis was performed with UPD of Cu(II) occurring on the MoS2 surface (Figure 3.2), and second, electroless replacement of reduced Cu atoms with the more noble Pt(IV) (Figure 3.3) was carried out. Based on the current response during the UPD step, it appears that any adsorption takes place within a few seconds, since the current quickly reaches 0 A. Therefore, a 60 second runtime for this experiment may be much longer than necessary.

From the potential response during the electroless replacement step, it appears that potential is asymptotically approaching some value but not reaching it. This could indicate that a longer runtime or a higher solution concentration is necessary if optimization of this process is desired.

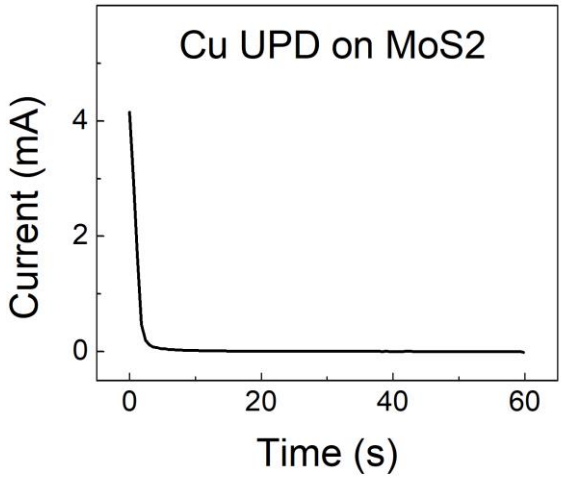

Figure 3.2 - Cu UPD on a sample of 30 nm MoS_2. Experimental runtime of 60 s with a constant applied potential of 0.12 V (vs Ag/AgCl).

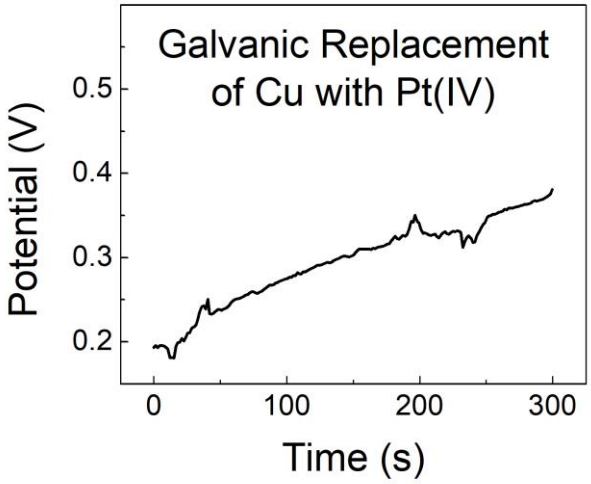

Figure 3.3 - Electroless replacement of adsorbed Cu with Pt(IV). Experiment runtime of 5 min. at OCP.

3.3.2 Surface chemistry

XPS characterization was performed on an array of Pt-ML/MoS_2 samples. As displayed in Table 3.1, these included samples synthesized by nine iterations of SLRR on a 30 nm MoS_2 film, three iterations of SLRR on a 30 nm MoS_2 film, and nine iterations of SLRR on a 1 nm MoS2 film. High-resolution scans of the Pt4f, S2p, Mo3d, and Ta4f peaks were performed for these samples. Figure 3.4 displays the $Pt4f_{7/2}$ and $Pt4f_{5/2}$ peaks. There is a shift in peak position of ~1.1 eV between the three samples with Pt appearing more cationic with fewer ML deposited and more like bulk metal as the number of ML increases on 30 nm MoS_2. However, even the sample with more Pt deposited is shifted to a more positive chemical state by ~0.2 eV from typical bulk Pt. This indicates that even with the deposition of ~4.5 ML of Pt, the substrate continues to influence the chemical state of Pt overlayers, and the threshold where influence from the support is no longer felt has not yet been reached. It appears in Figure 3.4(a) that the 1 nm MoS_2 sample has no Pt present on the surface, but closer analysis (Figure 3.4b) indicates that a much smaller amount exists compared to the 30 nm MoS_2 samples. The peak positions also mirror those of the sample with three SLRR iterations on 30 nm MoS_2, indicating that Pt exists in a more cationic state. This is presumably because the Pt is only going down at the edge sites on the MoS_2 and little or none is going down on the basal planes which, in this case, are parallel to the Ta foil substrate. Therefore, the amount of Pt deposited on the horizontally aligned, 1 nm thick MoS2 film was likely representative of the number of available edge sites, and the same holds true for the vertically aligned, 30 nm thick MoS_2. From this I infer that the quantity and location of Pt deposition via SLRR is directly influenced by the alignment of the MoS_2. This also brings up the interesting possibility of whether the Pt is going down in

wetted films, nucleating at the edge sites, which may be acting as anchor points for the metal atoms, or depositing in some combination of wetted films and nanoparticles.

It is also interesting to observe that Pt peaks appear clearly bimodal, independent of Pt film thickness. It was conceivable that Pt on MoS_2 would show additional XPS peaks representing the presence of multiple oxidation states for a thinner film thickness. Instead, the shifted and well defined peak doublet, suggests the presence of a single oxidation state that is simply shifted due to the degree that the MoS_2 support influences the surface Pt atoms.

Table 3.1 – Array of Pt/MoS_2 samples produced for XPS characterization.

Base Material	MoS_2 Film Thickness	Number of SLRR Iterations	Targeted Number of Pt Monolayers
Bulk Ta Foil	30 nm	9	4.5
Bulk Ta Foil	30 nm	3	1.5
Bulk Ta Foil	1 nm	9	4.5

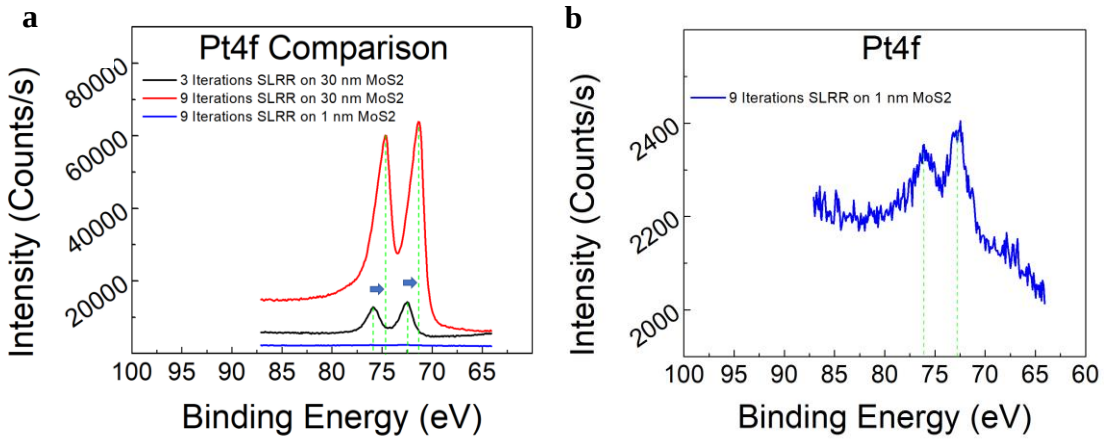

Figure 3.4 – XPS characterization of Pt on 30 nm and 1 nm MoS_2 films on bulk Ta foil. (a) Comparison of $Pt4f_{7/2}$ and $Pt4f_{5/2}$ peaks for samples synthesized with nine iterations of SLRR on 30 nm MoS_2, nine iterations of SLRR on 1 nm MoS_2, and 3 iterations of SLRR on 30 nm MoS_2. (b) $Pt4f_{7/2}$ and $Pt4f_{5/2}$ peaks for sample synthesized with nine iterations of SLRR on 1 nm MoS_2.

Comparing the XPS spectra from Mo3d5/2, Mo3d3/2, S2p3/2, and S2p1/2 yields additional, valuable information regarding the surface composition (Figure 5). The intensity of these peaks from the nine SLRR iterations on 30 nm MoS2 sample is significantly lower than the three SLRR iterations on 30 nm MoS2 sample. This signals both that (i) the quantity of Pt deposited on the surface is increasing with the number of SLRR iterations and (ii) the Pt coverage is uniform across the substrate surface. This finding is significant since one of the main goals of this work is to synthesize highly wetted thin films, and the XPS data discussed is evidence of just that. It should also be noted that there appears to be some degree of MoO3 present based on the peak at ~236 eV in Figure 3.5a. This is likely the result of either the electrodeposition process or XPS.

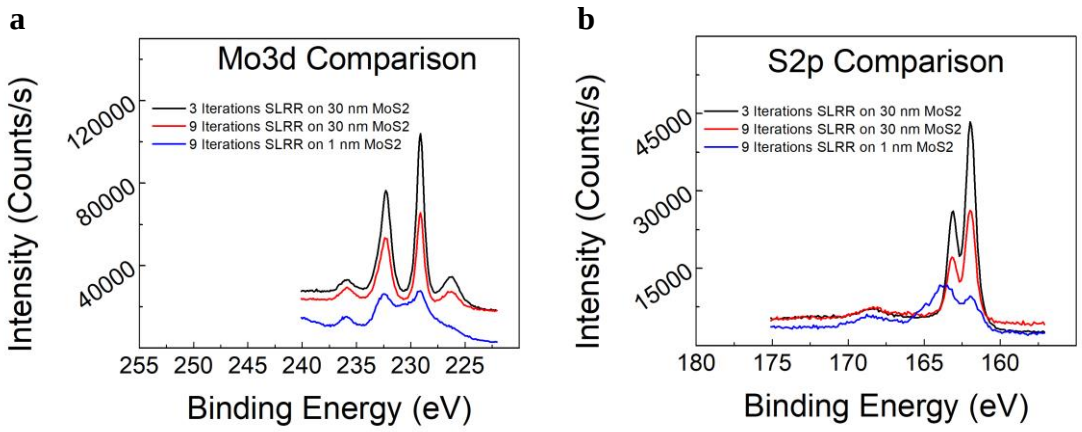

Figure 3.5 – XPS characterization of Mo and S from samples listed in Table 3.1. (a) Comparison of $Mo3d_{5/2}$ and $Mo3d_{3/2}$ peaks. (b) Comparison of $S2p_{3/2}$, and $S2p_{1/2}$ peaks.

3.3.3 Electrochemical Characterization

Cyclic voltammetry was used to evaluate the material after Pt deposition. A 0.1 M H_2SO_4 electrolyte solution was used and purged with N_2 before testing. The potential could not be increased enough to oxidize Pt without damaging the MoS_2, and therefore, the success of Pt deposition was confirmed by presence or absence of hydrogen "waves". Figure 3.6 provides an example voltammogram from this type of characterization.

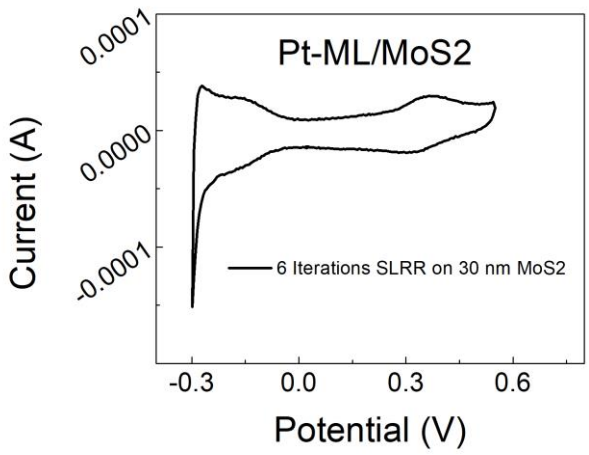

Figure 3.6 – Cyclic voltammogram for MoS_2 film of thickness 30 nm with Pt deposited on the surface through six iterations of SLRR. Sweep rate was 50 mV/s and reference electrode was Ag/AgCl

Electrocatalytic characterization was carried out by running HER in a three-electrode cell filled with 0.1 M H2SO4. One proposed reaction pathway for the HER reaction consists of four steps (Equations 3.1, 3.2, 3.3, and 3.4) (subscripts A represents a lower energy surface site and subscript B represents a higher energy surface site). [64] For this experiment LSV was performed at a starting potential of 0.3 V (vs Ag/AgCl) with a sweep rate of 20 mV/s. The comparison between samples produced with Pt on 5 nm, Pt on 30 nm MoS_2, and Pt foil (**Error! Reference source not found.**) yields some interesting i nformation regarding the influence of MoS_2 on Pt overlayers. It appears that the concentration of available MoS_2 edge sites influences the performance of Pt-ML/MoS_2 as a catalyst for HER. This finding provides helps to confirm that Pt is being deposited at the edge sites of MoS_2 and not the basal planes.

$$H^+ + e^- \rightleftharpoons H_{ads,A} \quad (3.1)$$

$$H_{ads,A} \rightarrow H_{ads,B} \quad (3.2)$$

$$2H_{ads,B} \rightarrow H_2 \quad (3.3)$$

$$H_{ads,A\ or\ B} + H^+ + e^- \longrightarrow H_2 \quad (3.4)$$

Furthermore, it appears that HER performance varies greatly with the amount of Pt deposited, but only about 4 monolayers of precious metal are necessary before catalytic performance mirrors bulk Pt foil. Comparison of Tafel slopes agrees with this assessment (Figure 3.7). The reaction kinetics of the sample synthesized by nine iterations of SLRR on 30 nm MoS_2 match those of Pt foil. The kinetics of HER on the samples synthesized with three iterations of SLRR are clearly different, based on the Tafel slopes, but the overpotentials vary greatly between the two samples. This is likely a consequent of fewer available edge sites on the 5 nm MoS_2 sample compared to the 30 nm sample. The change in Tafel slopes may also indicate a change in the rate limiting step for the HER reaction pathway. Chen et al. suggest that surface diffusion of H_{ads} can take the place of H_2 desorption as the rate limiting step in HER. [64]

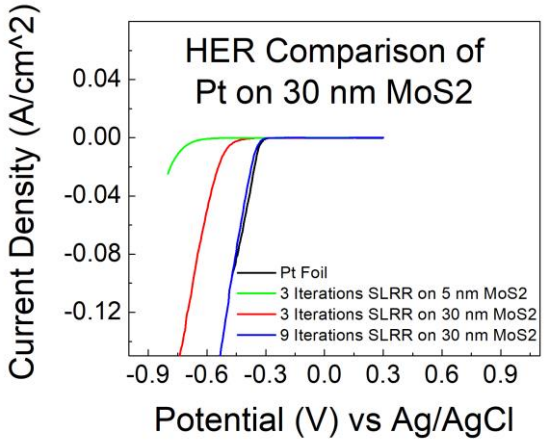

Figure 3.8 - HER comparison of between samples of Pt on 5 nm and 30 nm MoS_2 films, Pt foil, and 30 nm MoS_2 without Pt. The electrolyte solution contained 0.1 M H_2SO_4 and a sweep rate of 20 mV/s was used.

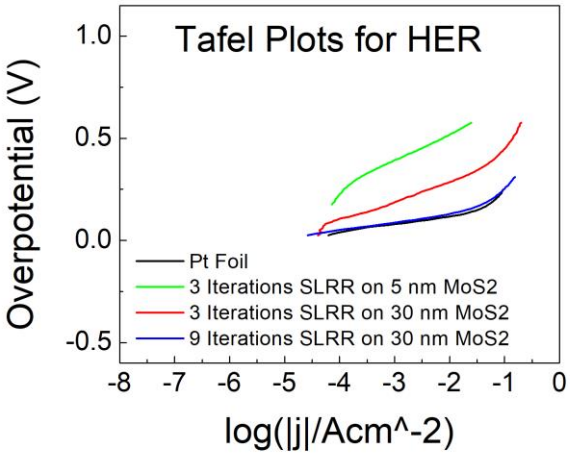

Figure 3.7 - Tafel plots comparing catalytic activity catalysts for the HER. Catalysts consist of Pt foil, and variations of Pt on MoS_2.

Table 3.2 – Comparison of Tafel slopes for HER reaction on various catalysts

Sample Types	Tafel Slope (V/decade)
Pt Foil	0.0388
3 Iterations SLRR on 5 nm MoS_2	0.1283
3 Iterations SLRR on 30 nm MoS_2	0.1031
9 Iterations SLRR on 30 nm MoS_2	0.0383

3.4 Summary

These results indicate that SLRR can be applied for deposition of well dispersed Pt films at the exposed edge sites of MoS2. Additionally, the chemical state of Pt on MoS_2 can be tuned as a function of Pt layer thickness, with the targeted 4.5 Pt-ML possessing a chemical state similar to bulk Pt and thinner Pt films acting more cationic. Characterization of catalytic performance endorses the finding that interaction between Pt and MoS_2 tunes electric and chemical properties of Pt, since thicker Pt films on 30 nm MoS_2 performed similarly to Pt foil in terms of HER activity. Hence, SLRR can be utilized for the precious control of Pt loading on the surface of MoS_2 and fine-tuning of the catalyst's activity. Both of these being highly sought-after characteristics in the area of electrocatalysis. That being said, additional work is needed to observe the manner in which Pt deposits on the MoS_2 surface. It is unclear, based on these findings, whether Pt is going down in atomically thin films or more of nanoparticle films.

CHAPTER 4. CONCLUSIONS AND FUTURE DIRECTIONS

4.1 Conclusions

This work presents pathways, based on SLRR, for depositing Pt nanostructures on two distinct substrates. The first, a graphene foam with and without a Ni interior showed potential for Pt-ML growth and opens the door for synthesizing enhanced nanostructured catalysts in a 3D way. This work has shown that the enhancement in activity over that of a commercial Pt/C catalyst is derived from the metal ligand effect between the Ni skeleton and Pt-ML. This interaction between Ni and Pt was able to occur despite the presence of a graphene capping layer, approximately 1 nm thick, on the Ni surface. Additionally, this work presents a method for etching away the Ni interior of foam while maintaining Pt-ML on the graphene surface. This process offers the potential for incorporation of a new metal substrate, delivering a ligand flexible catalyst.

The second substrate utilized for Pt deposition in this thesis was MoS_2 film ranging in thickness from 1 to 30 nm. By attempting Pt microstructure deposition on this surface via SLRR I attempted to ascertain information on the influence of MoS_2 edge sites on achieving highly-wetted ML of precious metal as well as its effect on the electronic properties of Pt nanostructures. While it is clear that the concentration of available edge sites has a dramatic effect on Pt deposition, the exact organization of Pt atoms has yet to be discerned. XPS and electrochemical characterization revealed that MoS_2 influences the chemical state of Pt when the film remains below a certain thickness threshold, but again, follow up research is needed to determine if this is an effect of charge transfer or strained Pt lattice growth. Overall these results demonstrate that MoS_2 can be used as a substrate

for tuning the activity of Pt nanostructures as a function of available edge sites and quantity of Pt deposited, but additional research is necessary to further investigate the root causes of initial conclusions.

4.2 Future Directions

There are certainly still some barriers that need to be addressed before introducing any of the catalysts discussed in this work into more realistic applications. Determining the durability of precious metal monolayers on graphene and MoS_2 was outside the scope of this work, but is critical in applications with harsh operating environments such as PEM fuel cells. There is potential that the Pt-ML would succumb to degradation such as Ostwald ripening or dissolution, and even more likely is that dissolution of the Ni skeleton, in the case of the 3D graphene catalyst, would occur in low pH environments. [65] All of these outcomes, would unquestionably impact the activity of these catalysts in a negative manner.

Important as well, is the follow up work necessary to determine the manner in which MoS_2 impacts Pt overlayers. Advanced characterization techniques such as TEM, XAS, and EXAFS would likely be needed to glean the information needed to ascertain the exact manner in which MoS_2 influences the Pt electronic structure.

In addition, this work did not explore the deposition of other precious metals on either the graphene or MoS_2. It would be interesting to determine whether other metals arrange in similar fashions on the surfaces of these substrates and whether the support would have an equivalent impact on catalyst performance. There is evidence, in research from other

groups, to suggest that Pt is more likely to agglomerate than other precious metals. [28] Therefore, other metals may form more uniform ML.

Finally, the foam structure could use significant optimization. Our work, less focused on optimizing the concept, worked with commercially available microporous Ni foams. To truly take advantage of the scalability this substrate offers, the Ni branch and foam pore size should be altered to allow for the greatest possibly interfacial area without impeding the graphene growth and Pt deposition processes.

REFERENCES

[1] A. Abdelhafiz, A. Vitale, C. Joiner, E. Vogel and F. M. Alamgir, "Layer-by-layer evolution of structure, strain, and activity for the oxygen evolution reaction in graphene-templated Pt monolayers," *ACS Applied Materials and Interfaces,* vol. 7, no. 11, pp. 6180-6188, 2015.

[2] J. K. Nørskov, J. Ressmeisl, A. Logadottir, L. Lindqvist, J. R. Kitchin, T. Bligaard and H. Jonsson, "Origin of the overpotential for oxygen reduction at a fuel cell cathode," *J. Phys. Chem. B,* vol. 108, pp. 17886-17892, 2004.

[3] J. Zhang, PEM fuel cell electrocatalysts and catalyst layers: Fundamentals and applications, 2008.

[4] K. Kim, J. Y. Choi, T. Kim, S. H. Cho and H. J. Chung, *A role for graphene in silicon-based semiconductor devices,* vol. 479, 2011, pp. 338-344.

[5] C. N. Rao, A. K. Sood, K. S. Subrahmanyam and A. Govindaraj, *Graphene: The new two-dimensional nanomaterial,* vol. 48, 2009, pp. 7752-7777.

[6] N. Shang, P. Papakonstantinou, P. Wang and S. R. P. Silva, "Platinum integrated graphene for methanol fuel cells," *Journal of Physical Chemistry C,* vol. 114, no. 37, pp. 15837-15841, 2010.

[7] A. K. Geim and K. S. Novoselov, "The rise of graphene," *Nature Materials,* vol. 6, no. 3, pp. 183-191, 2007.

[8] M. S. A. Bhuyan, M. N. Uddin, M. M. Islam, F. A. Bipasha and S. S. Hossain, "Synthesis of graphene," *International Nano Letters,* vol. 6, no. 2, pp. 65-83, 2016.

[9] S. Bae, H. Kim, Y. Lee, X. Xu, J. S. Park, Y. Zheng, J. Balakrishnan, T. Lei, H. Ri Kim, Y. I. Song, Y. J. Kim, K. S. Kim, B. Özyilmaz, J. H. Ahn, B. H. Hong and S. Iijima, "Roll-to-roll production of 30-inch graphene films for transparent electrodes," *Nature Nanotechnology,* vol. 5, no. 8, pp. 574-578, 2010.

[10] C. Lee, X. Wei, J. W. Kysar and J. Hone, "Measurement of the elastic properties and intrinsic strength of monolayer graphene," *Science,* vol. 321, no. 5887, pp. 385-388, 2008.

[11] K. S. Novoselov, A. K. Geim, S. Morozov, D. Jiang, Y. Zhang, S. V. Dubonos, I. V. Grigorieva and A. A. Firsov, "Electric Field Effect in Atomically Thin Carbon Films," *Science,* vol. 306, no. 5696, pp. 666-669, 2004.

[12] A. A. Balandin, S. Ghosh, W. Bao, I. Calizo, D. Teweldebrhan, F. Miao and C. N. Lau, "Superior thermal conductivity of single-layer graphene," *Nano Letters,* vol. 8, no. 3, pp. 902-907, 2008.

[13] A. Eftekhari and H. Garcia, *The necessity of structural irregularities for the chemical applications of graphene,* vol. 4, 2017, pp. 1-16.

[14] I. Fampiou and A. Ramasubramaniam, "Binding of Pt nanoclusters to point defects in graphene: Adsorption, morphology, and electronic structure," *Journal of Physical*

Chemistry C, vol. 116, no. 11, pp. 6543-6555, 2012.

[15] D. Chen, H. Feng and J. Li, *Graphene oxide: Preparation, functionalization, and electrochemical applications,* vol. 112, 2012, pp. 6027-6053.

[16] A. Kumar and Q. Xu, *Two-Dimensional Layered Materials as Catalyst Supports,* vol. 4, 2018, pp. 28-40.

[17] X. Huang, Z. Zeng, S. Bao, M. Wang, X. Qi, Z. Fan and H. Zhang, "Solution-phase epitaxial growth of noble metal nanostructures on dispersible single-layer molybdenum disulfide nanosheets," *Molecular therapy : the journal of the American Society of Gene Therapy,* vol. 4, p. 1444, 2013.

[18] L. H. Yuwen, F. Xu, B. Xue, Z. M. Luo, Q. Zhang, B. Q. Bao, S. Su, L. X. Weng, W. Huang and L. H. Wang, "General synthesis of noble metal (Au, Ag, Pd, Pt) nanocrystal modified MoS2 nanosheets and the enhanced catalytic activity of Pd-MoS2 for methanol oxidation," *Nanoscale,* vol. 6, no. 11, pp. 5762-5769, 2014.

[19] S. H. Patil, B. Anothumakkool, S. D. Sathaye and K. R. Patil, "Architecturally designed Pt–MoS_2 and Pt–graphene composites for electrocatalytic methanol oxidation," *Phys. Chem. Chem. Phys.,* vol. 17, no. 39, pp. 26101-26110, 2015.

[20] C. Du, H. Lin, B. Lin, Z. Ma, T. Hou, J. Tang and Y. Li, "MoS_2 supported single platinum atoms and their superior catalytic activity for CO oxidation: a density functional theory study," *J. Mater. Chem. A,* vol. 3, no. 46, pp. 23113-23119, 2015.

[21] Y. Wang, B. Wang, R. Huang, B. Gao, F. Kong and Q. Zhang, "First-principles study of transition-metal atoms adsorption on MoS2monolayer," *Physica E: Low-Dimensional Systems and Nanostructures,* vol. 63, pp. 276-282, 2014.

[22] H. A. Gasteiger, S. S. Kocha, B. Sompalli and F. T. Wagner, *Activity benchmarks and requirements for Pt, Pt-alloy, and non-Pt oxygen reduction catalysts for PEMFCs,* vol. 56, 2005, pp. 9-35.

[23] K. Kinoshita, "Particle Size Effects for Oxygen Reduction on Highly Dispersed Platinum in Acid Electrolytes," *Journal of The Electrochemical Society,* vol. 137, no. 3, p. 845, 1990.

[24] J. X. Wang, H. Inada, L. Wu, Y. Zhu, Y. M. Choi, P. Liu, W. P. Zhou and R. R. Adzic, "Oxygen reduction on well-defined core-shell nanocatalysts: Particle size, facet, and Pt shell thickness effects," *Journal of the American Chemical Society,* vol. 131, no. 47, pp. 17299-17302, 2009.

[25] V. R. Stamenkovic, B. Fowler, B. S. Mun, G. Wang, P. N. Ross, C. A. Lucas and N. M. Markovic, "Improved oxygen reduction activity on Pt3Ni(111) via increased surface site availability," *Science,* vol. 315, no. 5811, pp. 493-497, 2007.

[26] V. Stamenkovic, B. S. Mun, K. J. Mayrhofer, P. N. Ross, N. M. Markovic, J. Rossmeisl, J. Greeley and J. K. Nørskov, "Changing the Activity of Electrocatalysts for Oxygen Reduction by Tuning the Surface Electronic Structure," *Angewandte Chemie International Edition,* vol. 45, no. 18, pp. 2897-2901, 2006.

[27] R. Reske, H. Mistry, F. Behafarid, B. Roldan Cuenya and P. Strasser, *Particle size effects in the catalytic electroreduction of CO2 on Cu nanoparticles,* vol. 136, 2014, pp. 6978-6986.

[28] K. A. Friedrich, A. Marmann, U. Stimming, W. Unkauf and R. Vogel, "Model

electrodes with defined mesoscopic structure," *Fresenius' Journal of Analytical Chemistry,* vol. 358, no. 1-2, pp. 163-165, 1997.

[29] H. F. Waibel, M. Kleinert, L. A. Kibler and D. M. Kolb, "Initial stages of Pt deposition on Au(111) and Au(100)," *Electrochimica Acta,* vol. 47, no. 9, pp. 1461-1467, 2002.

[30] S. R. Brankovic, J. X. Wang and R. R. Adžić, "Metal monolayer deposition by replacement of metal adlayers on electrode surfaces," *Surface Science,* vol. 474, no. 1-3, pp. L173-L179, 2001.

[31] D. M. Kolb, M. Przasnyski and H. Gerischer, "Underpotential deposition of metals and work function differences," *Journal of Electroanalytical Chemistry,* vol. 54, no. 1, pp. 25-38, 1974.

[32] V. Sudha and M. V. Sangaranarayanan, "Underpotential deposition of metals – Progress and prospects in modelling," *Journal of Chemical Sciences,* vol. 117, no. 3, pp. 207-218, 2005.

[33] V. Sudha and M. V. Sangaranarayanan, "Underpotential deposition of metals: Structural and thermodynamic considerations," *Journal of Physical Chemistry B,* vol. 106, no. 10, pp. 2699-2707, 2002.

[34] Y. G. Kim, J. Y. Kim, D. Vairavapandian and J. L. Stickney, "Platinum nanofilm formation by EC-ALE via redox replacement of UPD copper: Studies using in-situ scanning tunneling microscopy," *Journal of Physical Chemistry B,* vol. 110, no. 36, pp. 17998-18006, 2006.

[35] M. Fayette, Y. Liu, D. Bertrand, J. Nutariya, N. Vasiljevic and N. Dimitrov, "From Au to Pt via surface limited redox replacement of Pb UPD in one-cell configuration," *Langmuir,* vol. 27, no. 9, pp. 5650-5658, 2011.

[36] S. Koh and P. Strasser, "Electrocatalysis on bimetallic surfaces: Modifying catalytic reactivity for oxygen reduction by voltammetric surface dealloying," *Journal of the American Chemical Society,* vol. 129, no. 42, pp. 12624-12625, 2007.

[37] T. Bligaard and J. K. Nørskov, "Ligand effects in heterogeneous catalysis and electrochemistry," *Electrochimica Acta,* vol. 52, no. 18, pp. 5512-5516, 2007.

[38] R. E. Rettew, S. Cheng, M. Sauerbrey, T. A. Manz, D. S. Sholl, C. Jaye, D. A. Fischer and F. M. Alamgir, "Near surface phase transition of solute derived Pt monolayers," in *Topics in Catalysis*, 2013.

[39] D. Gokcen, S.-E. Bae and S. R. Brankovic, "Stoichiometry of Pt Submonolayer Deposition via Surface-Limited Redox Replacement Reaction," *Journal of The Electrochemical Society,* vol. 157, no. 11, p. D582, 2010.

[40] S. Cheng, R. E. Rettew, M. Sauerbrey and F. M. Alamgir, "Architecture-dependent surface chemistry for Pt monolayers on carbon-supported Au," *ACS Applied Materials and Interfaces,* vol. 3, no. 10, pp. 3948-3956, 2011.

[41] P. Strasser, S. Koh, T. Anniyev, J. Greeley, K. More, C. Yu, Z. Liu, S. Kaya, D. Nordlund, H. Ogasawara, M. F. Toney and A. Nilsson, "Lattice-strain control of the activity in dealloyed core-shell fuel cell catalysts," *Nature Chemistry,* vol. 2, no. 6, pp. 454-460, 2010.

[42] M. K. Min, J. Cho, K. Cho and H. Kim, "Particle size and alloying effects of Pt-

based alloy catalysts for fuel cell applications," *Electrochimica Acta,* vol. 45, no. 25-26, pp. 4211-4217, 2000.

[43] M. Mavrikakis, B. Hammer and J. K. Nørskov, "Effect of strain on the reactivity of metal surfaces," *Physical Review Letters,* vol. 81, no. 13, pp. 2819-2822, 1998.

[44] J. Zhang, M. B. Vukmirovic, Y. Xu, M. Mavrikakis and R. R. Adzic, "Controlling the catalytic activity of platinum-monolayer electrocatalysts for oxygen reduction with different substrates," *Angewandte Chemie - International Edition,* vol. 44, no. 14, pp. 2132-2135, 2005.

[45] V. Stamenković, T. J. Schmidt, P. N. Ross and N. M. Marković, "Surface composition effects in electrocatalysis: Kinetics of oxygen reduction on well-defined Pt3Ni and Pt3Co alloy surfaces," *Journal of Physical Chemistry B,* vol. 106, no. 46, pp. 11970-11979, 2002.

[46] U. a. Paulus, a. Wokaun, G. G. Scherer, P. S. Institut and C.-. V. Psi, "Oxygen Reduction on Carbon-Supported Pt - Ni and Pt - Co Alloy Catalysts," *Journal of Physical Chemistry B,* vol. 106, no. 41, pp. 4181-4191, 2002.

[47] H. Yano, M. Kataoka, H. Yamashita, H. Uchida and M. Watanabe, "Oxygen reduction activity of carbon-supported Pt-M (M = V, Ni, Cr, Co, and Fe) alloys prepared by nanocapsule method," *Langmuir,* vol. 23, no. 11, pp. 6438-6445, 2007.

[48] H. Yang, W. Vogel and C. Lamy, "Structure and Electrocatalytic Activity of Carbon-Supported Pt - Ni Alloy Nanoparticles Toward the Oxygen Reduction Reaction," *Journal Physical Chemistry B,* vol. 108, pp. 11024-11034, 2004.

[49] J. Zhang, H. Yang, J. Fang and S. Zou, "Synthesis and Oxygen Reduction Activity of Shape-Controlled Pt 3 Ni Nanopolyhedra," *Nano Letters,* vol. 10, no. 2, pp. 638-644, 2010.

[50] L. G. Santos, C. H. Oliveira, I. R. Moraes and E. A. Ticianelli, "Oxygen reduction reaction in acid medium on Pt-Ni/C prepared by a microemulsion method," *Journal of Electroanalytical Chemistry,* vol. 596, no. 2, pp. 141-148, 2006.

[51] T. Y. Jeon, S. J. Yoo, Y. H. Cho, K. S. Lee, S. H. Kang and Y. E. Sung, "Influence of oxide on the oxygen reduction reaction of carbon-supported Pt-Ni alloy nanoparticles," *Journal of Physical Chemistry C,* vol. 113, no. 45, pp. 19732-19739, 2009.

[52] V. R. Stamenkovic, B. S. Mun, K. J. Mayrhofer, P. N. Ross and N. M. Markovic, "Effect of surface composition on electronic structure, stability, and electrocatalytic properties of Pt-transition metal alloys: Pt-skin versus Pt-skeleton surfaces," *Journal of the American Chemical Society,* vol. 128, no. 27, pp. 8813-8819, 2006.

[53] T. He, E. Kreidler, L. Xiong, J. Luo and C. J. Zhong, "Alloy electrocatalysts - Combinatorial discovery and nanosynthesis," *Journal of the Electrochemical Society,* vol. 153, no. 9, pp. A1637-A1643, 2006.

[54] T. Y. Jeon, S. K. Kim, N. Pinna, A. Sharma, J. Park, S. Y. Lee, H. C. Lee, S. W. Kang, H. K. Lee and H. H. Lee, "Selective Dissolution of Surface Nickel Close to Platinum in PtNi Nanocatalyst toward Oxygen Reduction Reaction," *Chemistry of Materials,* vol. 28, no. 6, pp. 1879-1887, 2016.

[55] Z. Chen, W. Ren, L. Gao, B. Liu, S. Pei and H. M. Cheng, "Three-dimensional

flexible and conductive interconnected graphene networks grown by chemical vapour deposition," *Nature Materials,* vol. 10, no. 6, pp. 424-428, 2011.

[56] A. C. Ferrari, J. C. Meyer, V. Scardaci, C. Casiraghi, M. Lazzeri, F. Mauri, S. Piscanec, D. Jiang, K. S. Novoselov, S. Roth and A. K. Geim, "Raman spectrum of graphene and graphene layers," *Physical Review Letters,* vol. 97, no. 18, 2006.

[57] L. Baraton, Z. B. He, C. S. Lee, C. S. Cojocaru, M. Chtelet, J. L. Maurice, Y. H. Lee and D. Pribat, "On the mechanisms of precipitation of graphene on nickel thin films," *EPL,* vol. 96, no. 4, 2011.

[58] A. Abdelhafiz, V. Adam, P. Buntin, B. deGlee, C. Joiner, A. Robertson, V. M. Eric, J. Warner and F. M. Alamgir, "Epitaxial and atomically thin graphene–metal hybrid catalyst films: the dual role of graphene as the support and the chemically-transparent protective cap," *Energy Environ. Sci.,* 2018, Advance Article, DOI: 10.1039/C8EE00539G.

[59] D. Prasai, J. C. Tuberquia, R. R. Harl, G. K. Jennings and K. I. Bolotin, "Graphene: Corrosion-inhibiting coating," *ACS Nano,* vol. 6, no. 2, pp. 1102-1108, 2012.

[60] I. Mintsouli, J. Georgieva, E. Valova, S. Armyanov, A. Kakaroglou, A. Hubin, O. Steenhaut, J. Dille, A. Papaderakis, G. Kokkinidis and S. Sotiropoulos, "Pt-Ni carbon-supported catalysts for methanol oxidation prepared by Ni electroless deposition and its galvanic replacement by Pt," *Journal of Solid State Electrochemistry,* vol. 17, no. 2, pp. 435-443, 2013.

[61] N. P. Kondekar, M. G. Boebinger, E. V. Woods and M. T. McDowell, "In Situ XPS Investigation of Transformations at Crystallographically Oriented MoS2Interfaces," *ACS Applied Materials and Interfaces,* vol. 9, no. 37, pp. 32394-32404, 2017.

[62] Y. Jung, J. Shen, Y. Liu, J. M. Woods, Y. Sun and J. J. Cha, "Metal seed layer thickness-induced transition from vertical to horizontal growth of MoS2and WS2," *Nano Letters,* vol. 14, no. 12, pp. 6842-6849, 2014.

[63] D. Kong, H. Wang, J. J. Cha, M. Pasta, K. J. Koski, J. Yao and Y. Cui, "Synthesis of MoS2 and MoSe2 films with vertically aligned layers," *Nano Letters,* vol. 13, no. 3, pp. 1341-1347, 2013.

[64] A. Kahyarian, B. Brown and S. Nesic, "Mechanism of the Hydrogen Evolution Reaction in Mildly Acidic Environments on Gold," *Journal of The Electrochemical Society,* vol. 164, no. 6, pp. H365-H374, 2017.

[65] H. R. Colón-Mercado, H. Kim and B. N. Popov, "Durability study of Pt3Ni1 catalysts as cathode in PEM fuel cells," *Electrochemistry Communications,* vol. 6, no. 8, pp. 795-799, 2004.

[66] H. He and C. Gao, "Graphene nanosheets decorated with Pd, Pt, Au, and Ag nanoparticles: Synthesis, characterization, and catalysis applications," *Science China Chemistry,* vol. 54, no. 2, pp. 397-404, 2011.